Zambrano, M., Tondi, E., Mancini, L., Lanzafame, G., Trias, F. X., Arzilli, F., Materazzi, F., Torrieri, S. (2018) Fluid flow simulation and permeability computation in deformed porous carbonate grainstones. *Advances in water resources*, Maig 2018, vol. 115, p. 95-111. DOI: <10.1016/j.advwatres.2018.02.016>.

FLUID FLOW SIMULATION AND PERMEABILITY COMPUTATION IN DEFORMED POROUS CARBONATE GRAINSTONES

M. Zambrano [1,2,*], E. Tondi [1,2], L. Mancini [3], F. Arzilli [3,4], G. Lanzafame [3], M. Materazzi [1], S. Torrieri [1,5], F.X. Trias [6]

1. School of Science and Technology - Geology Division, University of Camerino, Italy.

2. Reservoir Characterization Project (www.rechproject.com)

3. Elettra-Sincrotrone Trieste S.C.p.A., Basovizza (Trieste), Italy

4. School of Earth and Environmental Sciences, University of Manchester, Oxford Road, Manchester, M13 9PL, UK

5. Shell Italia Exploration and Production, Italy.

6. Heat and Mass Transfer Technological Center, Polytechnic University of Catalonia. Terrassa (Barcelona) Spain.

*Corresponding author: Miller Zambrano

Corresponding author affiliation: School of Science and Technology - Geology Division, University of Camerino. Via Gentile III da Varano 1, 62032 Camerino, Italy.

E-mail: miller.zambrano@unicam.it

Abstract

In deformed porous carbonates, the architecture of the pore network may be modified by deformation or diagenetic processes varying the permeability with respect to the pristine rock. The effects of the pore texture and morphology on permeability in porous rocks have been widely investigated due to the importance during the evaluation of geofluids reservoirs. In this study, these effects are assessed by combining synchrotron X-ray computed microtomography (SR micro-CT) and computational fluid dynamics. The studied samples pertain to deformed porous carbonate grainstones highly affected by deformation bands (DBs) exposed in Northwestern Sicily and Abruzzo regions, Italy.

The high-resolution SR micro-CT images of the samples, acquired at the SYRMEP beamline of the Elettra - Sincrotrone Trieste laboratory (Italy), were used for simulating a pressure-driven flow by using the lattice-Boltzmann method (LBM). For the experiments, a multiple relaxation time (MRT) model with the D3Q19 scheme was used to avoid viscosity-dependent results of permeability. The permeability was calculated by using the Darcy's law once steady conditions were reached. After the

simulations, the pore-network properties (porosity, specific surface area, and geometrical tortuosity) were calculated using the lattice velocity 3D images. Which were segmented considering a velocity threshold value higher than zero.

The study showed that DBs represents important heterogeneity features which generate significant permeability anisotropy. Cataclasis and cementation process taking place within the DBs reduce the effective porosity and therefore the permeability. Contrary, pressure dissolution and faulting may generate connected channels which contribute to the permeability only parallel to the DB.

Keywords: *Deformation bands; tortuosity; porosity; synchrotron X-ray computed microtomography; lattice-Boltzmann Method.*

Highlights:

- An MRT-LBM was used for obtaining viscosity-independent permeability in deformed carbonates.
- The influence of the pore-network morphology on the permeability was investigated.
- Fault core shows important heterogeneity and permeability anisotropy in comparison to the host rock.

1. Introduction

During the evaluation and development of geofluid reservoirs (water or hydrocarbons), one of the most elusive aspects is obtaining relationships between porosity and permeability. The permeability-porosity cross plots typically show important variability, which may indicate that permeability depends not only on the porosity but also on textural and hydraulic properties of the pore network such as pores size distribution, pores shape, and tortuosity (Carman, 1937; Dullien, 1992; Lucia, 2007).

Different attempts have been made to relate the pore-network properties and the permeability in order to describe their control or estimate the value of permeability (e.g. Kozeny, 1927; Carman, 1937; Archie, 1942; Wyllie and Rose, 1950; Swanson, 1981; and Katz and Thompson, 1986). One of the most widely used indirect methods for estimating the permeability is based on the so-called Kozeny-Carman (K-C) equation (Kozeny, 1927; Carman, 1937):

$$k = \frac{\phi^3}{\beta\,\tau^2\,S^2} \qquad \text{(equation 1)}$$

Where ϕ is the effective porosity, S is the specific surface area (depending on grain size and texture), τ is the tortuosity (here defined as the ratio of the actual length of fluid path divided by the Euclidean distance), and ?? is a pore shape factor normally rounded to 5.

The K-C equation is widely applied to estimate the permeability of realistic rock samples (e.g. Cerepi *et al.*, 2001; Agosta *et al.*, 2007) or fictitious rocks (Adler *et al.*, 1990). Adler *et al*. (1990) described the flow in complex pore geometries in modelled porous media based on statistical analysis thin section of homogeneous sandstones. These authors also found that the permeability values estimated with the Kozeny-Carman equation was significantly lower than permeability measured in laboratory. According to Dullien (1992), the K-C equation is often not valid in the following cases: i) when grains strongly deviate from the spherical shape, ii) when grains show a broad size distribution, or ii) when the grains are consolidated. Therefore, the K-C equation may be not valid for instance to estimate the permeability in deformed or diagenetic carbonates. A possible source of error in the implementation of the K-C equation is that its variables are often indirectly measured (Dullien, 1992; Wildenschild and Sheppard, 2013).

The direct flow simulations are currently widely used to calculate single phase flow and transport in complex porous media (Blunt *et al*., 2013; Bultreys *et al*., 2016, and references therein). Transport in rocks have been studied directly on realistic 3D pore space (obtained by X-ray tomographic, nuclear magnetic resonance), on reconstructed models from 2-D thin section images, and fictitious models. The three classical computational fluid dynamics approaches used for simulating fluid flow in porous media are: i) the finite difference method (Stapf *et al*., 2000; Øren and Bakke, 2002; Bijeljic *et al*., 2011; Mostaghimi *et al*., 2012; Bijeljic *et al*., 2013; Blunt *et al*., 2013), ii) the finite element method (Cardenas, 2008, 2009; Mostaghimi *et al*., 2013), and iii) the finite volume method (Zhang *et al*., 2012; Peng *et al*., 2014). In addition to these techniques, the lattice-Boltzmann method (LBM) is widely used for modeling flow in complex geometries (Dunsmuir *et al*, 1991; Chen and Doolen, 1998; Manz *et al*., 1999; Kang *et al*., 2006; Manwart *et al*., 2002; Sukop *et al.*, 2008; Porter *et al*., 2009; Schaap *et al*., 2007; Pan *et al*., 2004; Pan *et al.*, 2006; Hao and Cheng, 2010; Boek and Venturoli, 2010; Landry *et al*., 2014; Yang *et al.*, 2016).

The LBM describes the flow of a large number of particles interacting with the medium and among themselves following the Navier-Stokes equation at the macroscopic scale (Ladd, 1994). The LBM can handle complex pore geometry without any simplification and accurately describes fluid flow in porous media (Ladd, 1994; Keehm *et al.*, 2001). Pan *et al.* (2006) quantitatively evaluated the capability and accuracy of the LBM for modeling flow through two porous media, a body-centered cubic array of spheres and a random-sized sphere-pack. Yang *et al.* (2016) applied LBM and three other approaches (standard finite volume method, smoothed particle hydrodynamics, pore-network model) to simulate pore-scale velocity distributions and nonreactive solute transport. Sukop *et al.* (2008) used a parallel implementation of the three-dimensional Shan-and-Chen multicomponent, multiphase LBM to simulate the equilibrium distributions of two immiscible fluids in a quartz sand porous medium using cone-beam X-ray microtomography.

The LBM have been used to study the permeability on 3D images of rocks and soft sediments, obtained by micro-CT imaging techniques (Andrä *et al*., 2013; Fredrich *et al*., 2006; Khan *et al*., 2012; Manwart *et al*., 2002; Li *et al*., 2005; Degruyter *et al*., 2010; Shah *et al*., 2015) and from reconstructed models (Jin *et al*., 2004; Keehm, 2004; Wu *et al*., 2006). The computed permeability using the LBM has shown a good agreement with laboratory measurements over a wide range of permeability values (Keehm *et al.*, 2003, 2004). Manwart *et al*. (2002) compared the finite difference and the lattice Boltzmann approaches for calculating the permeability. These authors showed that the computation times and numerical results of the two methods were similar, however LBM is more memory demanding.

The simplest LBM is based on the Bhatnagar-Gross-Krook (BGK) collision operator, which consists in a single relaxation time approximation (Bhatnagar *et al.*, 1954). Using three-dimensional (3D) images at high spatial resolution collected at different synchrotron facilities, Degruyter *et al.* (2010) performed single phase gas simulations with the BGK-LBM and estimated the permeability in volcanic rocks by means of the software PALABOS (Latt, 2009). Ahrenholz *et al.* (2008) used the BGK-LBM to solve the coupled Navier–Stokes equations for two phases, to describe the dynamics of the fluid/fluid interface and to predict capillary hysteresis in a porous sand imaged with X-ray tomography. Despite its popularity, the BGK-LBM presents some drawbacks, for instance, the obtained permeability may be viscosity-dependent (Narvaez *et al.*, 2010). A more accurate alternative is the implementation of multiple relaxation times (MRT) methods, which are more stable and solve the drawbacks of the BGK method (e.g. d'Humières, 1992; d'Humières, *et al.* 2002). Pan *et al.* (2006) demonstrated that the MRT–LBM is superior to the BGK–LBM, and interpolation significantly improves the accuracy of the fluid–solid boundary conditions. MRT-LBM could be useful to implement experiments of multiple-phase flows. Zhang *et al.* (2016) used multi-relaxation time MRT-LBM to study the effect of the geometrical characteristics of bi-dimensional (2D) artificial porous media on the relative permeability in immiscible two-phase flows.

This work attempts to provide more evidence concerning the control exerted by the effective porosity, specific surface area and tortuosity on permeability in deformed carbonate rocks. This objective has been reached by combining quantitative images analysis and computational fluid dynamics using synchrotron radiation computed microtomography (SR micro-CT) images of deformed carbonate rock samples. The SR micro-CT images were acquired at the Elettra - Sincrotrone Trieste laboratory (Basovizza, Italy) and processed and analyzed as described by Zambrano *et al.* (2017). Due to the heterogeneity of the studied samples, different volumes of interest, containing pristine, deformed and diagenetized rocks, are analyzed to evaluate the effect of deformation on permeability. The permeability of deformed porous carbonate rocks was estimated via LBM, using the PALABOS open source library (Latt, 2009). The method and the code have been modified with respect to the work of Degruyter *et al.* (2010): the application of the MRT approach has been adopt in the present study rather than the BGK one in order to assure that values of permeability are viscosity-independent.

2. Methodology

2.1. Rock samples description

The samples selected for this study are from outcrops located in Sicily, southern Italy (Favignana Island and San Vito Lo Capo Peninsula; Fig. 1a, c) and Abruzzo Region, central Italy (Maiella Mt.; Fig. 1b, d), hereafter called San Vito Lo Capo Grainstone (SVG), Favignana Island Grainstone (FIG), and Orfento Fm. Grainstone (OFG), respectively. The studied rocks are different in terms of the grain composition, age and burial history. The SVGs (Early Pleistocene in age) are poor-to-medium consolidated grainstones with grains made up of fragments of carbonates, marls, and shales with a diameter between 0.05 and 1.0 mm. The matrix, about 22% of the rock volume, is composed of bladed and sparry calcite cement with carbonate and marl fragments smaller than 0.05 mm (Tondi, 2007). The Early Pleistocene FIGs consist of well-preserved bioclasts composed of *Vermetus*, *Serpula*, bivalves, echinoids, red algae and corals ranging in size from submillimeter to centimeter (Tondi *et al.*, 2012). The host rock is poorly cemented with the cement limited to the grain contacts, around echinoids, or within intragranular pores (Tondi *et al.*, 2012). The OFGs (Campanian to Maastrichtian in age) are composed of fragments of rudists (Mutti, 1995). The OFG experienced a maximum burial depth between 0.5 and 3 km (Ori *et al.*, 1986; Graham *et al.*, 2003; Rustichelli *et al.*, 2016), while both SVG and FIG experienced a shallower maximum burial depth of approximated 30 m (Tondi *et al.*, 2012; Antonellini *et al.*, 2014).

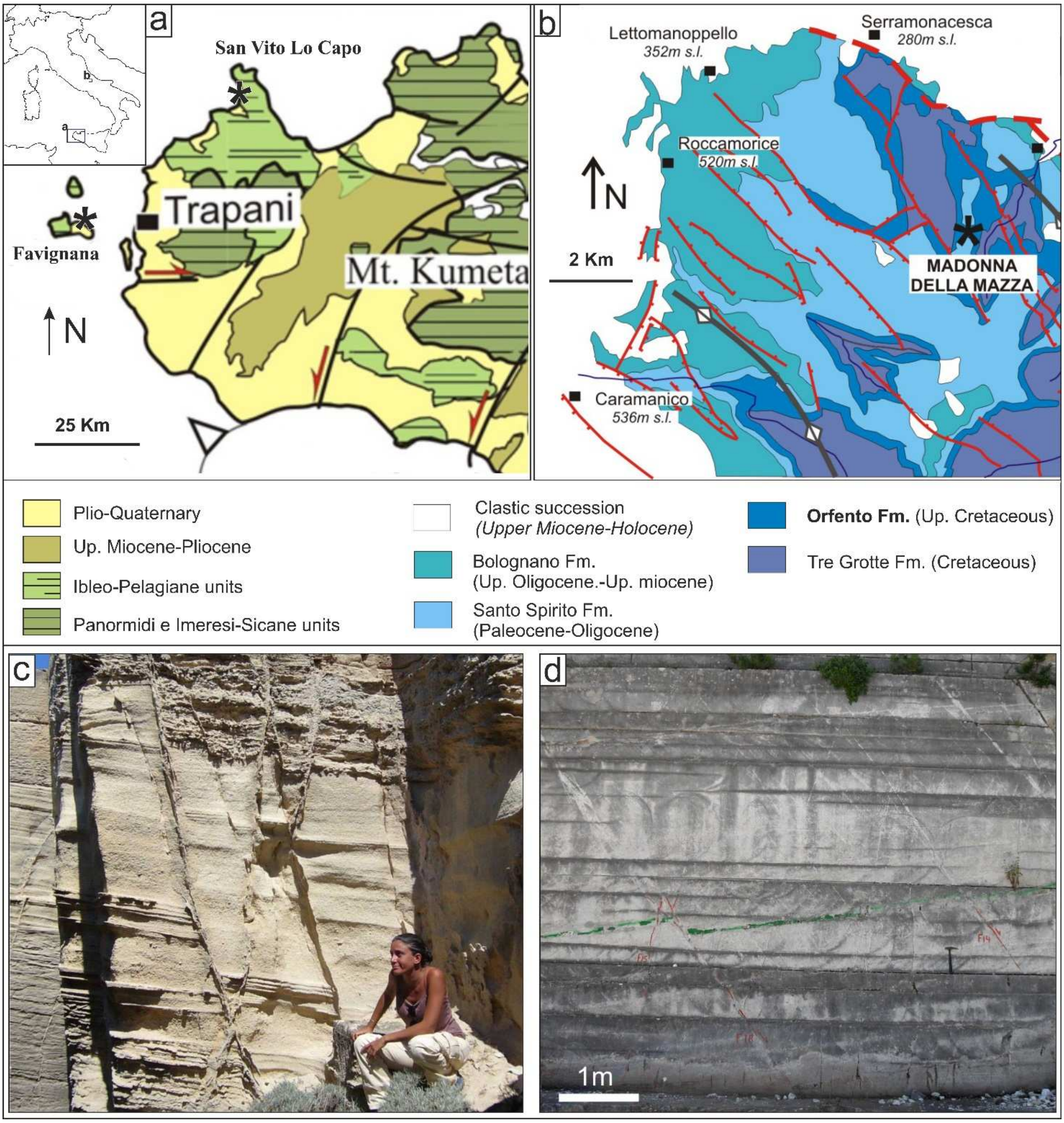

Figure 1. - Geological maps and location of the studied outcrops of a) Favignana Island and San Vito Lo Capo peninsula, and b) the northern part of the Maiella Mountain (modified from Tondi *et al.*, 2016). Outcrop images of the studied rocks showing both c) FIG and d) OFG crosscut by normal faults and compactive shear bands.

The studied samples may contain deformation bands (DBs), where strain localization (Aydin, 1978; Antonellini *et al.*, 1994; Fossen *et al.*, 2007; Cilona *et al.*, 2012, 2014) and chemical processes such as pressure solution and cementation (Hellman *et al.*, 2002; Tondi *et al.*, 2006; Tondi, 2007; Gaviglio *et al.*, 2009) may take place. Tondi *et al.* (2006) defined three diagenetic/structural tabular zones within the DBs (Zones I, II, III; Fig. 2) with different textures. Zones I and II are defined as the fault core of the deformation band (Tondi, 2007). Zone I (ZI), located at the inner part of the DB, includes the slip surfaces and a well-developed continuous zone of grain size and porosity reduction. Zone II (ZII), which limits the ZI, is a compacted grain zone characterized by pressure dissolution at the grain contacts. Zone III (ZIII) surrounds the fault core and is characterized by porosity reduction due to precipitation of calcite cement. Within DBs, the porosity and permeability are reduced considerably likely buffering for geofluid migration (Fossen and Bale, 2007; Tondi, 2007; Antonellini *et al.*, 2014; Tondi *et al.*, 2016).

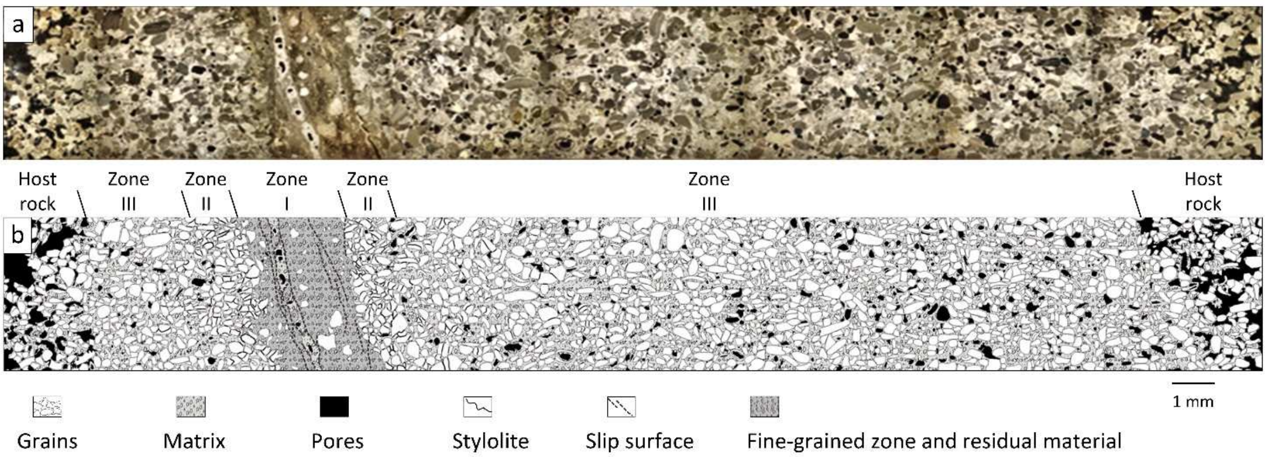

Figure 2. – Single deformation band from San Vito Lo Capo grainstone characterized by tabular zones (Zones I, II, and III) with different textures (see text for description) enclosed by the host rock; (a) microphotographs and (b) interpretation (after Tondi, 2007).

The permeability of the studied rocks has been previously assessed by Antonellini *et al.* (2014) and Tondi *et al.* (2016) in both host rock and DBs (including Zones I, II and III) using a TinyPerm II Portable Air permeameter (with a reliable range of 10^{-17} to 10^{-12} m^2). The surface was carefully cleaned and a silicon ring (5 mm of diameter) was used to avoid air leaking from the mini permeameter nozzle. These authors reported meaningful variability of permeability and porosity between host rock and the different zones within the DBs (Fig. 3). Tondi *et al.* (2016) pointed out that the permeability between FIG and OFG differs in the range of two-to-three orders of magnitude despite their similar porosity. Zambrano *et al.* (2017) inferred that the permeability differences between the grainstones pertaining to the distinct locations may be related to significant differences of connected porosity, specific surface area and connectivity.

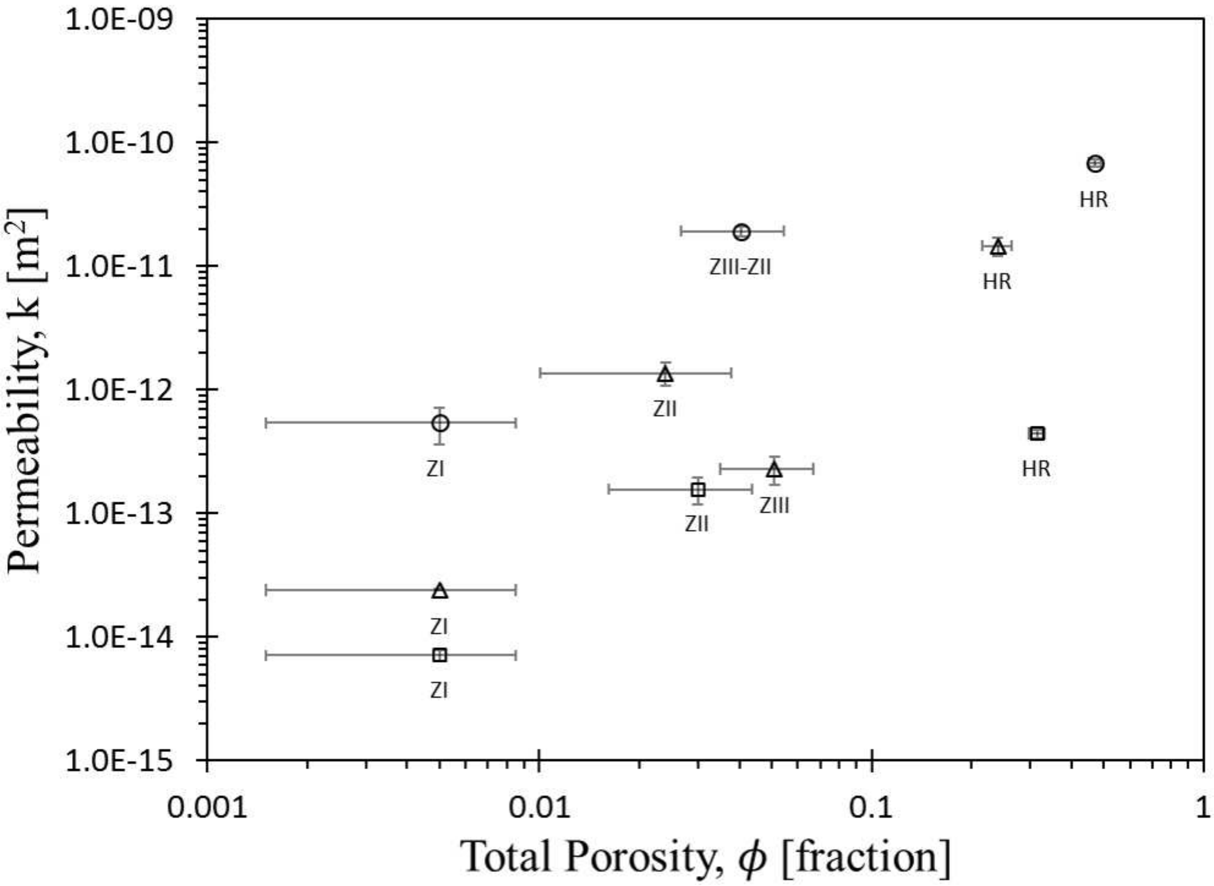

Figure 3. Scatterplot of porosity and permeability of the studied carbonate grainstones. Data of porosity for the SVG (triangles) from Tondi *et al.* (2007), for FIG (circles) from Tondi *et al.* (2012), and for OFG (squares) from Tondi *et al.* (2016). Data of permeability for the SVG Antonellini *et al.* (2014), and for both FIG and OFG from Tondi *et al.* (2016). Error bars correspond to the standard error of the mean. Both axes are in logarithmic scale. Meaning of acronyms are HR: host rock, ZI: zone I, ZII: zone II, ZIII: zone III.

For the SR micro-CT experiments, five parallelepiped-shaped samples (with size of ~ 4 mm x 4 mm x 30 mm) were selected from the studied SVG, FIG and OFG rocks (Fig. 4). From the SVG, the studied sample (SVG-S1) contains a compactive shear band composed of three different zones (I, II, III; *sensu* Tondi *et al.* 2006) surrounded by undeformed host rock. From the FIG two samples were collected; one of the host rock (FIG-S2) and one belonging to a fault core of about 5 centimeters in thickness (FIG-S3). From the OFG two samples were selected; one composed entirely of host rock (OFG-S4) and the other includes a single DB (OFG-S5).

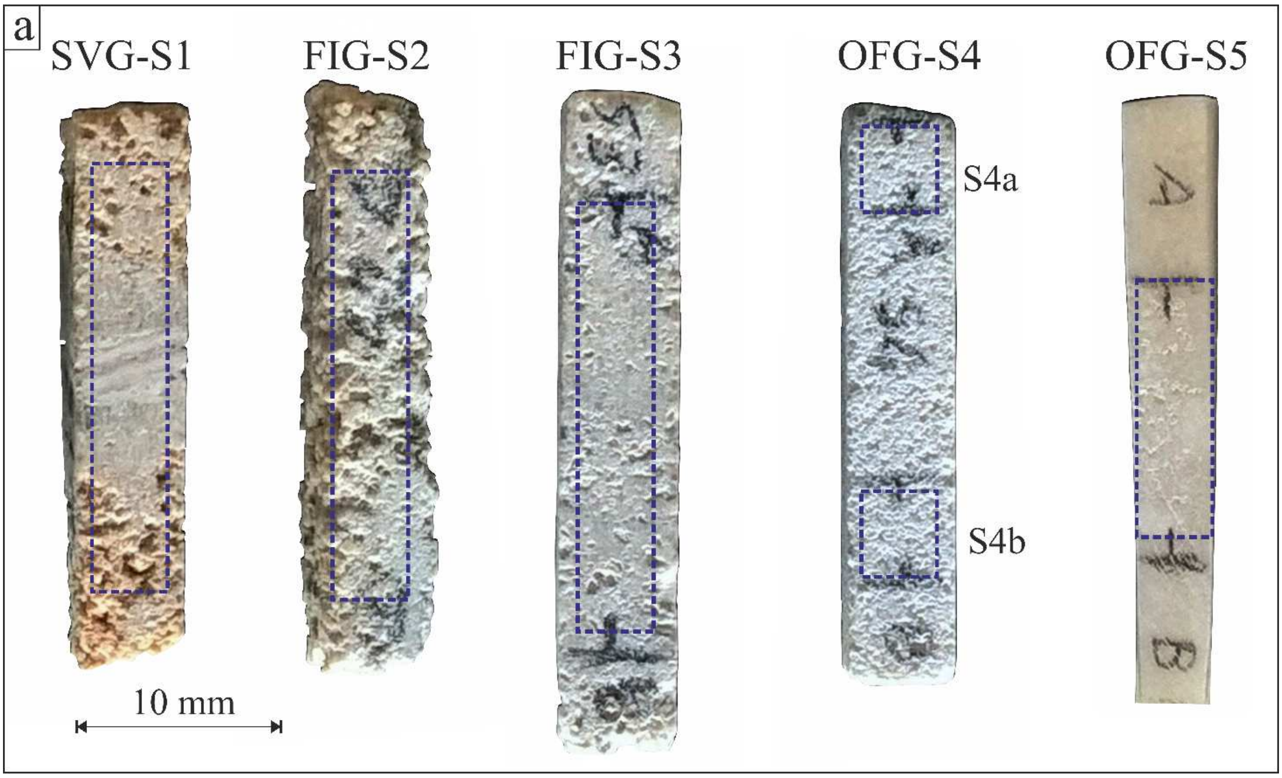

Figure 4. – Studied samples pertaining to deformed carbonate grainstones were obtained from outcrops located at northwestern Sicily (S1-S3) and Abruzzo (S4, S5) regions, Italy. a) Photograph of the original samples, the dotted areas correspond roughly to the imaged and analyzed volumes after removing the irregular edges. The longest axis of the samples is subparallel to bedding and orthogonal to the fault/DB zones (dipping 50º-90º, Tondi *et al.*, 2016).

2.2. Synchrotron radiation microtomography experiments

The SR micro-CT experiments and the image processing and analysis were performed following the methodology described by Arzilli *et al.* (2015) and Zambrano *et al*. (2017). The selected rock samples were imaged at the SYRMEP beamline of the Elettra laboratory. The X-ray beam delivered from a bending magnet source has a nearly-parallel geometry and a high spatial coherence (Abrami *et al.*, 2005; Tromba *et al.*, 2010) allowing to take advantage of phase contrast effects (Cloetens *et al.*, 1996). This beamline is suitable for obtaining 3D images of carbonate rocks and extracting valuable information about pores morphology, connectivity, and permeability at the pore scale (e.g. Gharbi and Blunt, 2012; Blunt *et al*., 2013; Bijeljic *et al*., 2013; Cilona *et al*., 2014; Arzilli *et al*., 2015; Zambrano *et al*., 2017).

Zambrano *et al.* (2017) obtained images at medium spatial resolution (voxel size = 9.0 μm) and high spatial resolution (voxel size = 2.4 μm) using the monochromatic and the white beam configuration of the beamline, respectively.

For the images acquired in the monochromatic beam configuration, the sample-to-detector distance was set to 180 mm (propagation-based phase-contrast mode) and an X-ray energy of 34 keV was selected by a double-crystal Si monochromator. Each sample was placed on a high-resolution rotation stage, and a series of 1800 radiographs (projections) were acquired over a total angular range of 180° with an exposure time/projection of 3.5 sec. Projections were acquired by using a water-cooled, 12-bit, 4008 x 2672 pixels CCD camera (VHR, Photonic Science) with an effective pixel size of 4.5 μm. The camera chip was coupled to a Gadox scintillator screen through a fiber optics taper in order to convert the X-ray into visible light. Applying a 2x2 binning to the detector pixels, an output pixel size of 9.0 μm x 9.0 μm was used for image acquisition.

A white beam configuration mode was used to image samples belonging to DBs or fault rock (Baker *et al.*, 2012) at higher spatial resolution, filtering the X-ray beam with 1.5 mm Si + 0.025 mm of Mo. The sample-to-detector distance was set at 150 mm. For each sample, 1800 projections were acquired over a total scan angle of 180° with an exposure time/projection of 2 s. The detector consisted of a 16 bit, air-cooled, sCMOS camera (Hamamatsu C11440-22C) with a 2048 × 2048 pixel chip. The effective pixel size of the detector was set at 2.4 μm × 2.4 μm, yielding a maximum field of view of about 5.0 mm × 5.0 mm.

The tomographic slice reconstruction was performed using the SYRMEP Tomo Project software developed at Elettra (Brun *et al.*, 2015) and powered by the ASTRA tomography toolbox (Palenstijn *et al.*, 2011) and TomoPy (Gürsoy *et al.* 2014). To improve the reliability of quantitative morphological analysis and enhance the contrast between solid and porous phase, a single-distance phase-retrieval algorithm was applied to the white beam projections (Fig. 4) using the Paganin's algorithm (Paganin et al., 2002) based on the Transport of Intensity Equation (TIE).

In the present work, the medium spatial resolution images were selected for the computational simulation. The criteria of this decision were made mainly based on the computational limitations, even though it may imply to do not take into account micro-pores in the simulations. Suitable volumes of interests (VOIs) were selected to assess the pore-network properties and estimate the permeability in host rock and DBs. The size of VOIs (see Table 1) was determined by the dimension of each evaluated region (i.e. host rock, ZI, II and III) within the sample. The whole imaged sample was included in the study in order to increase the representativeness of the results. In wide zones, such as the host rock, a high number of VOIs were evaluated, whereas, in thin zones, such as DBs, fewer VOIs with similar dimension were extracted.

The investigated VOIs images have a multiphase composition due to the content of voids, calcite grains, calcite cement, and silica grains (Zambrano *et al.*, 2017). For that reason, a 3D image segmentation was performed by the automatic multiphase k-means clustering algorithm (Hartigan, 1975; Hartigan and Wong, 1979), setting 3 to 4 classes of objects, depending on the sample. The segmentation was performed by using the *Pore3D* software library developed at Elettra (Brun *et al.*, 2010; Zandomeneghi *et al.*, 2010). Then, a 3D bilateral filter (Tomasi and Manduchi, 1998) was applied to the reconstructed data for smoothing the images and preserving edges. Results are binary images composed of voids and grains. After this, the tool 'Find Connected Structures' of the Fiji software (Schindelin *et al.*, 2012) was used for dividing the pore space into two components: i) connected pores and ii) isolated pores. For the simulations, only the connected pore networks were used for easing the computation.

Table 1. VOIs dimensions and description

Sample	VOIs	Vol. [mm^3]	Volume [Voxels]	Description
SVG-S1	1HR	23.33	400 x 400 x 200	Host rock
	2HR	23.33	400 x 400 x 200	Host rock
	3HR	23.33	400 x 400 x 200	Host rock
	4ZIII	27.99	400 x 400 x 240	Zone III, highly cemented
	5FC	34.99	400 x 400 x 300	Fault core, with a slip surface
	6ZIII	17.50	400 x 400 x 150	Zone III, highly cemented
	7HR	23.33	400 x 400 x 200	Host rock
	8HR	23.33	400 x 400 x 200	Host rock
FIG-S2	1HR	43.74	500 x 400 x 300	Host rock
	2HR	43.74	500 x 400 x 300	Host rock
	3HR	43.74	500 x 400 x 300	Host rock
	4HR	43.74	500 x 400 x 300	Host rock
	5HR	43.74	500 x 400 x 300	Host rock
	1CEM	39.37	400 x 450 x 300	Fault core, highly cemented
FIG-S3	2CEM	39.37	400 x 450 x 300	Fault core, highly cemented
	3MIX	39.37	400 x 450 x 300	Fault core, partially cemented
	4MIX	39.37	400 x 450 x 300	Fault core, partially cemented
	5CEM	39.37	400 x 450 x 300	Fault core, highly cemented
	6CEM	39.37	400 x 450 x 300	Fault core, highly cemented
	7MIX	39.37	400 x 450 x 300	Fault core, partially cemented
	8DISS	39.37	400 x 450 x 300	Fault core, affected by dissolution
OFG-S4	1HR	44.29	450 x 450 x 300	Host rock
	2HR	44.29	450 x 450 x 300	Host rock
OFG-S5	1HR	34.99	400 x 400 x 300	Host rock
	2MIX	34.99	400 x 400 x 300	Partially cemented zone
	3CEM	34.99	400 x 400 x 300	Highly cemented zone
	4MIX	34.99	400 x 400 x 300	Partially cemented zone
	5MIX	34.99	400 x 400 x 300	Partially cemented zone

2.3. Lattice-Boltzmann method and permeability calculation

Lattice-Boltzmann simulations were performed by means of the open-source computational fluid dynamics software PALABOS (Latt, 2009) using a modified version of the methodology previously described by Degruyter *et al.*, (2010). The methodology consists in imposing a simple-phase fluid flow through the segmented 3D images by maintaining a fixed pressure gradient between the inlet and outlet faces of the volume, the rest of the faces were padded. The interface pores-voids was converted to bounce-back boundary conditions. The main difference with the methodology proposed by Degruyter *et al.* (2010) is the replacement of the collisional operator BGK by an MRT (d'Humières *et al.*, 2002) with a D3Q19 lattice.

The simulation ended once the imposed steady state condition was reached (standard deviation of the average energy<10^{-4} after 1000 steps, Degruyter *et al.*, 2010). After that, the permeability component parallel to the imposed flow was calculated applying the Darcy's law,

$$\frac{\delta P}{\delta x} = \frac{\mu}{k} U, \qquad \text{(equation 2)}$$

where, $\delta P/\delta x$ is the pressure gradient, μ the fluid kinematic viscosity, and U the average fluid velocity per unit of area. The permeability was calculated, using the same procedure, in three orthogonal directions two parallel to the DBs (k_x and k_y) and the third one perpendicular to the DB (k_y). All the variables are handled in lattice units before the permeability calculation, results are transformed to real world units multiplying by the effective length of the voxel side in meters. To guarantee a flow in the laminar regime, and therefore the validity of Darcy's law, it was evaluated that the permeability keeps stable among different pressure gradients (Degruyter *et al.*, 2010). The obtained permeability values are not considered as absolute due to the possible source of error caused by the resolution of the micro-CT images and the few number of samples evaluated during the experiments.

2.4. Analysis of the effective pore-network properties

After the simulations, the resulting lattice velocity volumes were segmented with a single threshold (lattice velocity >0) for obtaining the effective pore space contributing to the flow. The 3D visualization of the output images was obtained by the volume rendering procedure, using the commercial software VGStudio MAX 2.0 (Volume Graphics) and the software Paraview (Ahrens *et al.* 2005). The assessment of the segmented pore space was made using the *Pore3D* software library, which has been optimized for quantitative examination of X-ray micro-CT images of porous media and multiphase systems and includes several modules, such as filtering, morphological, anisotropy and skeleton analysis. The analyzed properties were the effective porosity, the specific surface area, and the tortuosity in three directions (x, y, z) corresponding to the fluid flow experiments.

The effective porosity (Φ) here is defined as the ratio of the pore volume with a non-zero velocity and the total volume of the sample. The specific surface area (S) is defined as the ratio of the surface in contact with fluid and the total volume. The tortuosity (τ) has a vast number of definitions based on geometrical, hydraulic, electrical, and diffusion parameters (Ghanbarian *et al.*, 2012 and references therein). In this work, the method used to evaluate the tortuosity is based on the direct measurement of the shortest distance between two points in the pores (Gommes *et al.*, 2009). The geometrical tortuosity is calculated as $\tau = Lg/Le$, where Lg is the geodesic length defined as the shortest path connecting two points in the pore space, and Le is the Euclidean length (Soille, 1999; Dunsmuir *et al.*, 1991).

2.5. Representativeness evaluation of results

The representative elementary volume (REV) is defined as the volume in which the variability of a property (e.g., porosity, specific surface area, tortuosity, permeability) tends to decay significantly, enclosing a representative amount of the sample heterogeneity (Bear, 1972; Zandomeneghi *et al*., 2010). The REV must be sufficiently larger to include a considerable number of pores to permit the meaningful statistical average required in the continuum concept (Bear, 1972). Several authors have studied the existence and the dimensions of a REV for different porous materials (Zhang *et al*. 2000; Al-Raoush and Papadopoulos 2010; Mostaghimi *et al*. 2013). Zhang *et al*. (2000) introduced the term of a 'statistical REV' for heterogeneous media, which is defined as the volume beyond which the mean becomes approximately constant and the coefficient of variation (Cv, defined as the ratio of the arithmetic mean divided by the sample standard deviation) is lower than a threshold value (e.g. $Cv < 0.2$). Al-Raoush and Papadopoulos (2010) proposed that the determination of the REV should be determined using the porosity distribution over different volumes. Mostaghimi *et al*. (2013) investigated the existence and size of REV for samples of sandstones and carbonate rocks using permeability, specific surface area, and porosity. These authors estimated that the necessary size of REV for the permeability evaluation should be larger than that for porosity and specific surface area. In this work, the statistical REV approach proposed by Zhang *et al*. (2000) is used.

2.6. Single cylindrical-shape pore experiments

In order to quantify the effect of resolution on the evaluated properties, a cylindrical-shape fictitious pore of radius, r, was considered. Downscaling the resolution, the porosity, specific surface area and permeability were calculated from the images and compared with the analytical values. The permeability is analytically derived from combining the Poiseuille's Equation for flow through a cylinder pipe with the Darcy's Law for flow in porous media,

$$k = \frac{\pi\ r^2}{8} \qquad \text{(equation 3)}$$

The results are normalized by the analytical values and plotted against the pore radius expressed in terms of number of voxels. In this way the observations could be applicable to any pore radius.

3. Results

The results of the MRT-LBM simulations are the calculated permeability and the lattice velocity volumes (Fig. 5- 7). From the lattice velocity volumes additional properties were quantitatively analyzed including the effective porosity, specific surface area and tortuosity of the pore network contributing to the permeability of the host rock and DBs. The multidirectional (axes x, y, and z) results of both quantitative pore network analysis and permeability calculated with LBM simulation are summarized in Table 2. As it was stated in the methods section, for each zone (i.e. HR, ZI, ZII, ZIII) the average values corresponded to the arithmetic mean, in the case of k_z and k_y, or the to the harmonic mean, in the case of k_z. In specific cases, only one measurement was obtained due to the dimension of the analyzed zone. The results of the effective porosity, specific surface area, and tortuosity were plotted with the corresponding value of calculated (LBM) permeability (Fig. 8) with the intention of evaluating their respectively control on permeability. Data is divided in pristine rocks and fault zones to individuate the effect of deformation and diagenesis on the pore network and permeability within DBs. The combined control of these properties was evaluated considering the Kozeny-Carman equation (Fig. 8d), however the intention was not to test the accuracy of this equation.

3.1. MRT-LBM simulations

In the case of host rocks, the SVG (Fig 5b, d) and FIG (Fig. 6d) showed a combination of both wide and narrow conduits. In both velocity volumes, it is shown how the wider diameter of conduits allows the fluid to reach higher velocities in comparison to the narrow conduits. Differently, in the host rock pertaining to the OFG the pore-network is represented by a high number of very thin fluid conduits (Fig. 7c, e). The dimension of the pore diameter seems to be related to the specific surface area (Table 2), where the lower values correspond to the FIG and the higher values to OFG host rocks.

For sample SVG-S1, velocity volumes indicated that the fluid conduits within the DB are significantly fewer than those of the host rock. Within the cemented zone, ZIII, the fluid flow experiments failed due to the absence of a connected pore-network. Within the fault core (Fig. 5c), the fluid flow is negligible in a direction perpendicular to the DB. However, the fluid flow is present through the space generated by the distribution of asperities within the slip surfaces. This pore-network is characterized by wide and anastomose conduits that concentrated the fluid flow through the sharp discontinuity. Solution-enlarged stylolites may also represent secondary pathways for flow.

The obtained permeability shows significant differences between the HR and the different zones composing the DB (Zones III, II, I). The HR exhibited high and isotropic values of permeability. In the cemented zones, the permeability is negligible in all directions (e.g. SVG-S1, OFG-S5) due to the absence of connected pores (Fig. 10). Within the fault cores, the permeability decreases by nearly two orders of magnitude and sometimes presents important anisotropy. In the case of the fault core of SVG-S1 (composed by ZIII and I), the permeability component perpendicular to the DB is zero, whereas the permeability components parallel to the DB are possible thanks to the presence of channelized pore-network. In the case of FIG-S3, the fault core is characterized by alternation of zones affected by cementation and dissolution creating a highly heterogeneity and anisotropy. In the studied samples, the permeability component perpendicular to the DB is null for the fault cores.

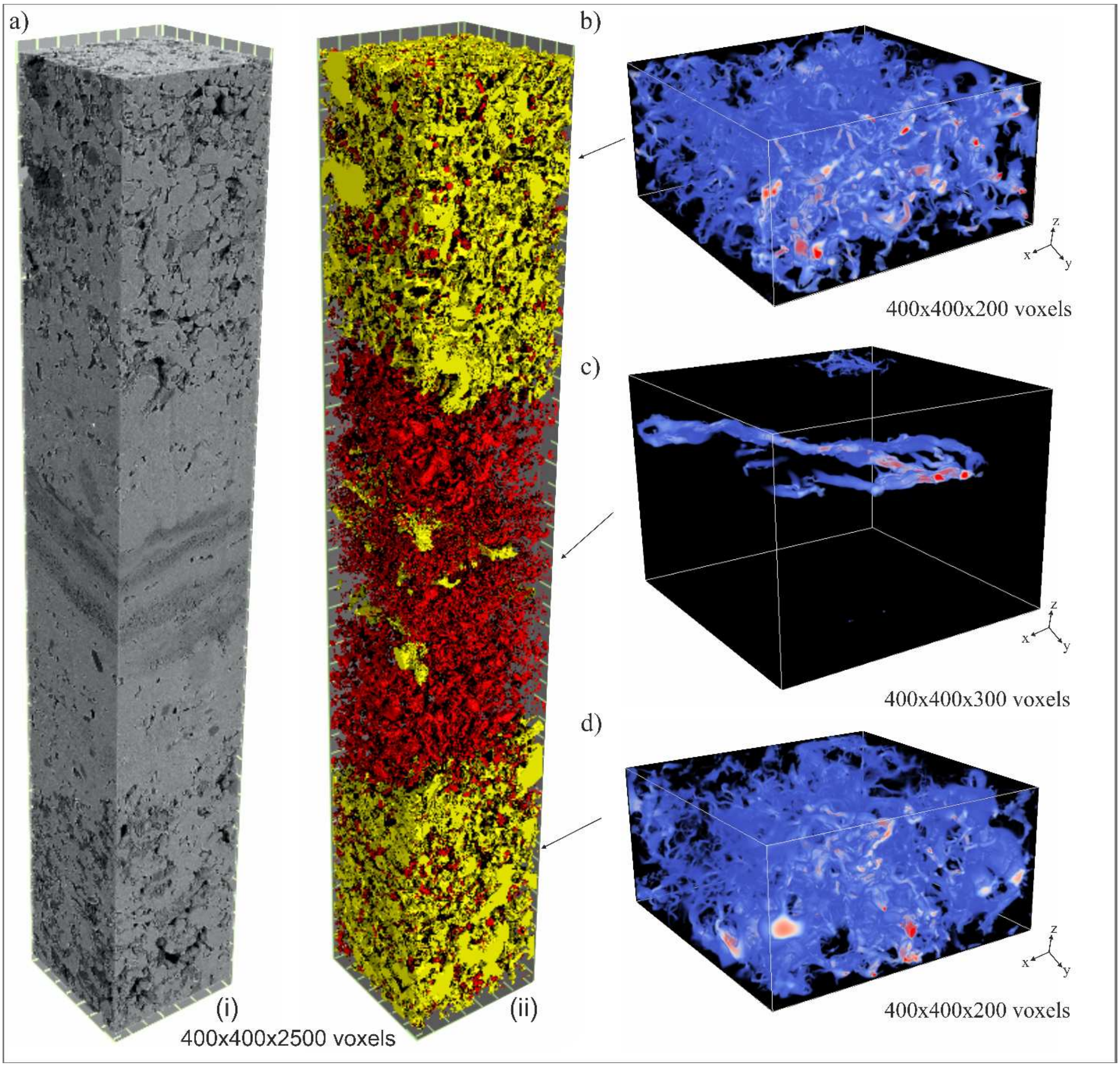

Figure 5.- a) Sample SVG-S1 with the volume rendering of the (i) raw reconstructed SR micro-CT images (voxel size = 9 µm) and (ii) segmented pores space (connected pores in yellow and unconnected pores in red, after Zambrano *et al.* 2017). Detail of lattice velocity volumes from the b) and d) host rock, and c) fault core. In the fluid velocity volumes, high velocities in lattice units are represented by warm colors. The z-axis of the volumes is perpendicular to the DB.

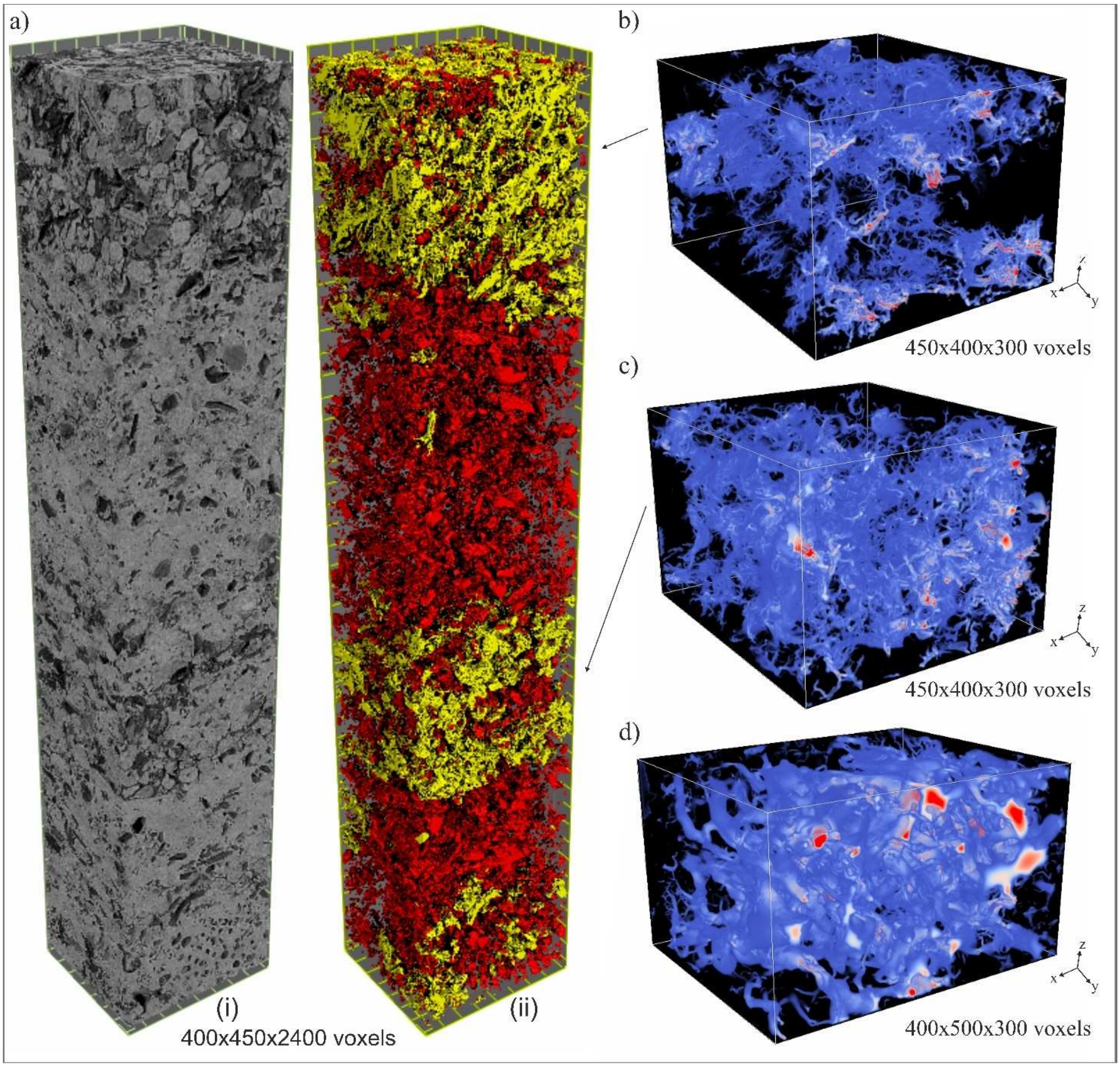

Figure 6.- a) Sample FIG-S3 with the rendering of the (i) raw reconstructed SR micro-CT images (voxel size = 9 µm) and (ii) segmented pores space (connected pores in yellow and unconnected pores in red, after Zambrano *et al.* 2017). Detail of lattice velocity volumes from the b) and c) fault core, and d) host rock from the sample FIG-S2. In the fluid velocity volumes, high velocities in lattice units are represented by warm colors. The z-axis of the volumes is perpendicular to the DB orientation.

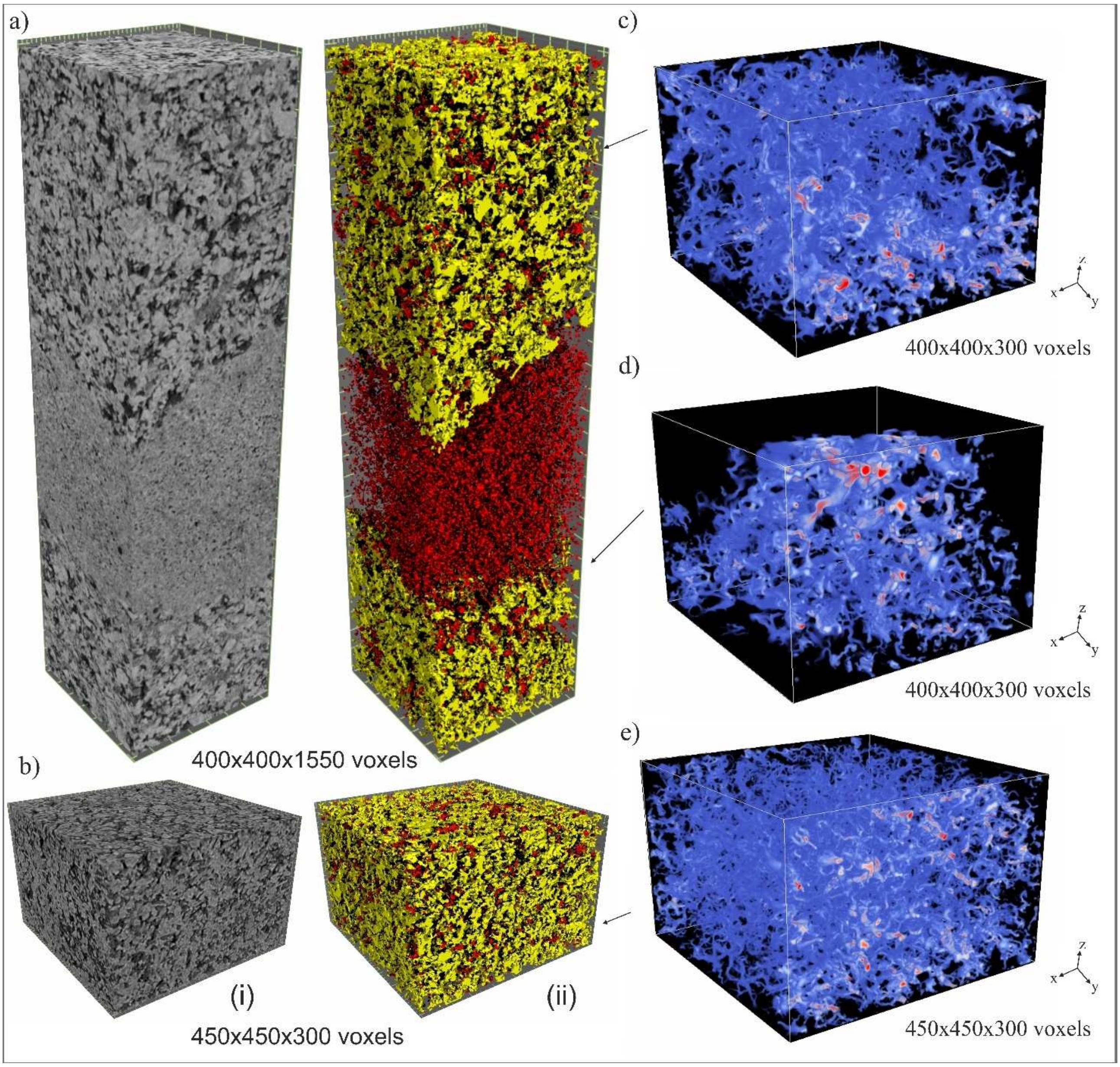

Figure 7.- a) Sample OFG-S5 (DB) and b) OFG-S4a (host rock) with the rendering of the (i) raw reconstructed SR micro-CT images (voxel size = 9 µm), and (ii) segmented pores space (connected pores in yellow and unconnected pores in red, after Zambrano *et al.* 2017). Detail of lattice velocity volumes from the c) host rock (near to the DB), e) host rock (far from DB), and d) transition between DB and host rock. In the fluid velocity volumes, high velocities in lattice units are represented by warm colors. The z-axis of the volumes is perpendicular to the DB orientation.

Table 2. Results of the quantitative pore network analysis and permeability calculation with LBM.

Sample	Zones		Φ_x [%]	Φ_y [%]	Φ_z [%]	S_x [mm^{-2}]	S_y [mm^{-2}]	S_z [mm^{-2}]	τ_x [-]	τ_y [-]	τ_z [-]	k_x [m^2]	k_y [m^2]	k_z [m^2]
SVG-S1	Host Rock	Mean	12.87	14.13	12.07	45.9	47.0	42.5	2.9	2.7	3.7	$9.5x10^{-13}$	$2.4x10^{-12}$	$2.3x10^{-12}$
		SE	0.69	0.28	0.52	4.6	5.7	3.4	0.4	0.1	0.4	$3.1x10^{-13}$	$8.7x10^{-13}$	$2.6x10^{-12}$
		Cv	0.09	0.03	0.07	0.17	0.21	0.14	0.30	0.06	0.25	0.57	0.64	1.06
	Zone III	Value	0.0	0.0	0.0	0.0	0.0	0.0	-	-	-	0.0	0.0	0.0
	Fault Core	Value	2.00	2.00	0.0	39.6	40.3	0.0	3.1	2.9	-	$3.0x10^{-13}$	$3.2x10^{-13}$	0.0
FIG-S2	Host Rock	Mean	26.15	26.55	28.10	28.8	28.6	29.6	1.6	1.9	1.9	$2.9x10^{-11}$	$6.0x10^{-11}$	$3.1x10^{-11}$
		SE	1.15	1.55	1.60	0.6	1.1	1.1	0.2	0.3	0.2	$1.3x10^{-11}$	$3.7x10^{-11}$	$2.0x10^{-11}$
		Cv	0.06	0.08	0.08	0.03	0.06	0.05	0.20	0.33	0.20	0.77	1.08	0.68
FIG-S3	Fault Core	Mean	5.19	5.36	2.11	35.1	35.4	7.2	3.1	3.8	2.2	$3.3 x10^{-13}$	$2.1 x10^{-13}$	0.0
		SE	2.13	2.13	2.11	14.5	14.7	7.2	0.1	0.2	1.6	$1.0 x10^{-13}$	$3.7x10^{-14}$	0.0
		Cv	1.09	1.07	2.65	1.02	1.02	2.65	0.10	0.12	1.03	0.81	0.46	2.8
OFG-S4	Host Rock	Mean	12.48	12.73	11.90	78.2	77.2	77.6	3.2	3.2	4.0	$4.0x10^{-13}$	$3.6x10^{-13}$	$4.2x10^{-13}$
		SE	0.91	0.97	0.53	1.7	2.0	1.7	0.1	0.2	0.2	$1.5x10^{-13}$	$6.8x10^{-14}$	$1.7x10^{-13}$
		Cv	0.145	0.13	0.09	0.043	0.045	0.044	0.045	0.15	0.11	0.73	0.33	0.52
OFG-S5	DB-	Mean	6.32	6.16	6.58	57.5	58.0	55.8	3.8	3.5	3.7	$2.6x10^{-13}$	$7.4x10^{-13}$	$2.1x10^{-13}$
		SE	1.88	1.84	1.38	0.9	1.0	2.5	0.3	0.3	0.3	$1.2x10^{-13}$	$2.6x10^{-13}$	$9.2x10^{-14}$
		Cv	0.67	0.67	0.47	0.033	0.034	0.10	0.16	0.20	0.17	1.01	0.79	0.60

3.2. Pore-network properties

All the evaluated host rocks showed a high effective porosity. The greatest effective porosity values in the host rock correspond to the FIG with a mean of 26.93 ± 0.75 %, followed by the SVG with a mean porosity of 13.02 ± 0.4 %, whereas the host rock of FIG showed a mean effective porosity of 12.33 ± 0.43 %. Within the DB hosted in SVG, the zones with high cementation, ZIII, are likely to have zero effective porosity, whereas, in the fault core with pore network composed of enlarge stylolites and slip surfaces, ZII and ZI respectively, the effective porosity is relative higher (about 2.0%). In the case of the fault core of FIG-S3, there is a high variability of effective porosity (Cv>1.0) due to the alternation of volumes affected by cementation or dissolution. VOIs is highly affected by cementation showed null porosity values, whereas in VOIs highly affected by dissolution the porosity could reach 15.1 %. Volumes partially cemented indicated a null porosity in the z-direction (perpendicular to the fault), whereas is about 7.26 ± 0.29 % for the other directions. Considering all the VOIs, the mean porosity tensor for the fault core sample FIG-S3 is Φ (5.19 ± 2.13 %; 5.36 ± 2.33

%; 2.11 ± 2.11 %). In the case of OFG-S5, some spot (with dimension lower than the VOIs) where well-cemented and presented null porosity. The mean porosity tensor for the OFG-S5 is Φ (1.88 ± 0.67 %; 1.84 ± 0.67 %; 1.38 ± 0.47 %). The coefficient of variation (Cv) showed values up to 0.67 for the porosity of this sample, which indicates an important heterogeneity. The scatter plot porosity-permeability (Fig. 8a) indicates an important control of the porosity on permeability and a clear differentiation between undeformed host rock and deformed/cemented zones.

The specific surface area indicates higher values for the host rock pertaining to OFG (77.71 ± 0.28 mm$^{-1)}$ in comparison to the host rocks of SVG (45.15 ± 0.80 mm^{-1}) and FIG (29.03 ± 0.19 mm^{-1}). In the case of DBs, the specific surface area could increase within the host rock in zones affected by dissolution and cataclasis as in FIG-S3 (about 60.0 mm^{-1}). Also, this could decrease is the dominant process is the cementation as in OFG-S5 (57.01 ± 0.28 mm^{-1}) or, in the extreme case, SVG-S1-ZIII characterized by high cementation and null effective porosity. As it was expected, the specific surface area seems to be inversely related to the permeability (Fig. 8b). However, there is not a clear differentiation of deformed and pristine rock possible related to the effect of deformation and diagenetic processes involved.

Concerning the geometrical tortuosity (Table 2), the values in the host rocks are 1.79 ± 0.04 for FIG, 3.07 ± 0.05 for SVG, and 3.46 ± 0.04 for OFG-S4. In the case of DBs, the geometric tortuosity could increase in the case of FIG-S3 (3.22 ± 0.08) and OFG-S5 (3.67 ± 0.04). The tortuosity seems to be inversely related to the permeability (Fig. 8c).

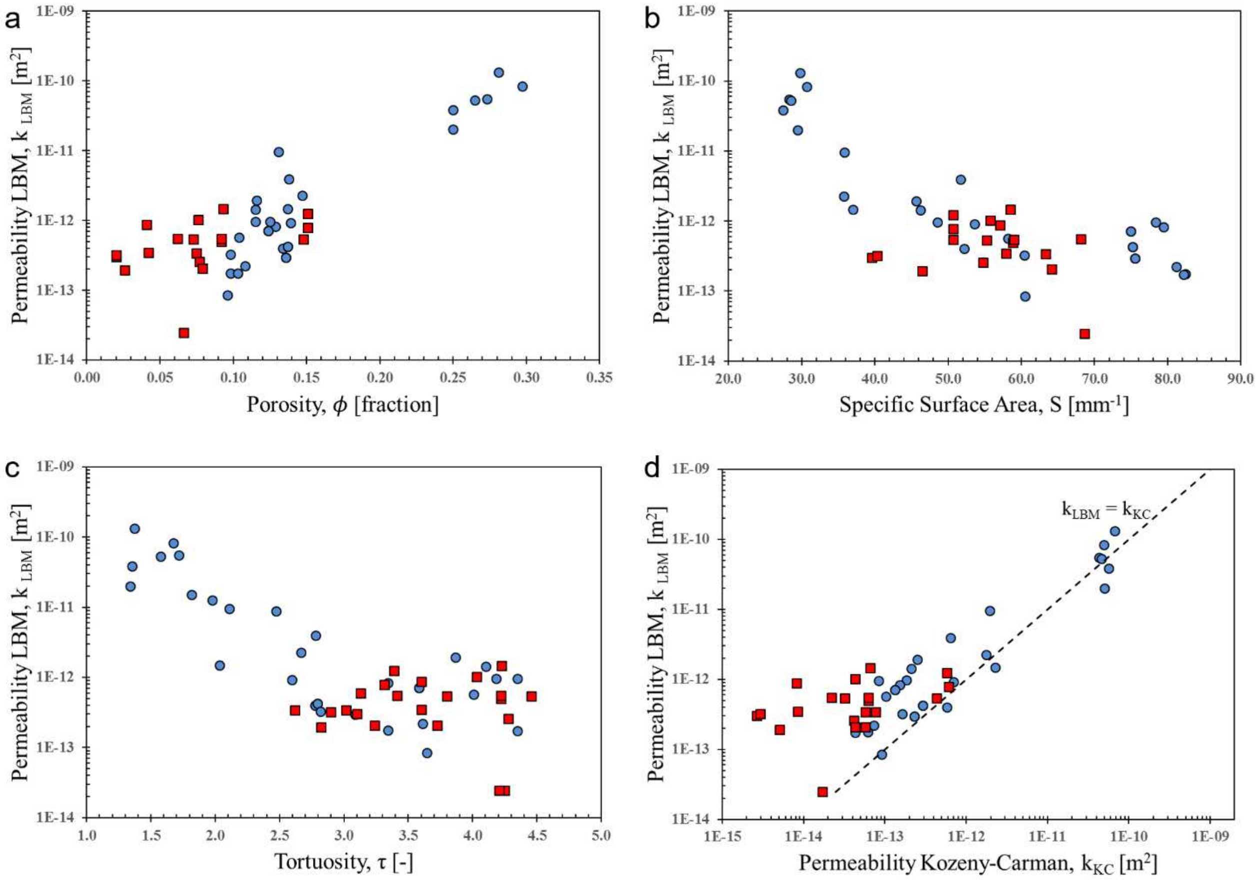

Figure 8. - Relationship between LBM permeability and a) effective porosity b) specific surface area c) geometrical tortuosity, and d) permeability estimated with the K-C equation. Host rock data is represented by blue circles, whereas deformed rock data is in red squares. In (d) the dotted line represents the equally between calculated (LBM) and estimated (K-C) permeability. The axis containing permeability data are in logarithmic scale.

3.3. Single cylindrical-shape pore experiments

The effect of resolution on the evaluated properties was assessed considering a single fictitious cylindrical-shape pore. Both porosity and specific surface are related to the resolution by a non-linear function (Figs. 9). For a pore with diameter represented by 10 voxels, both properties are less than 20% lower than the theoretical value. The permeability does not show significant variation (<10%) until the diameter of the pore is about 10 voxels (Fig. 9).

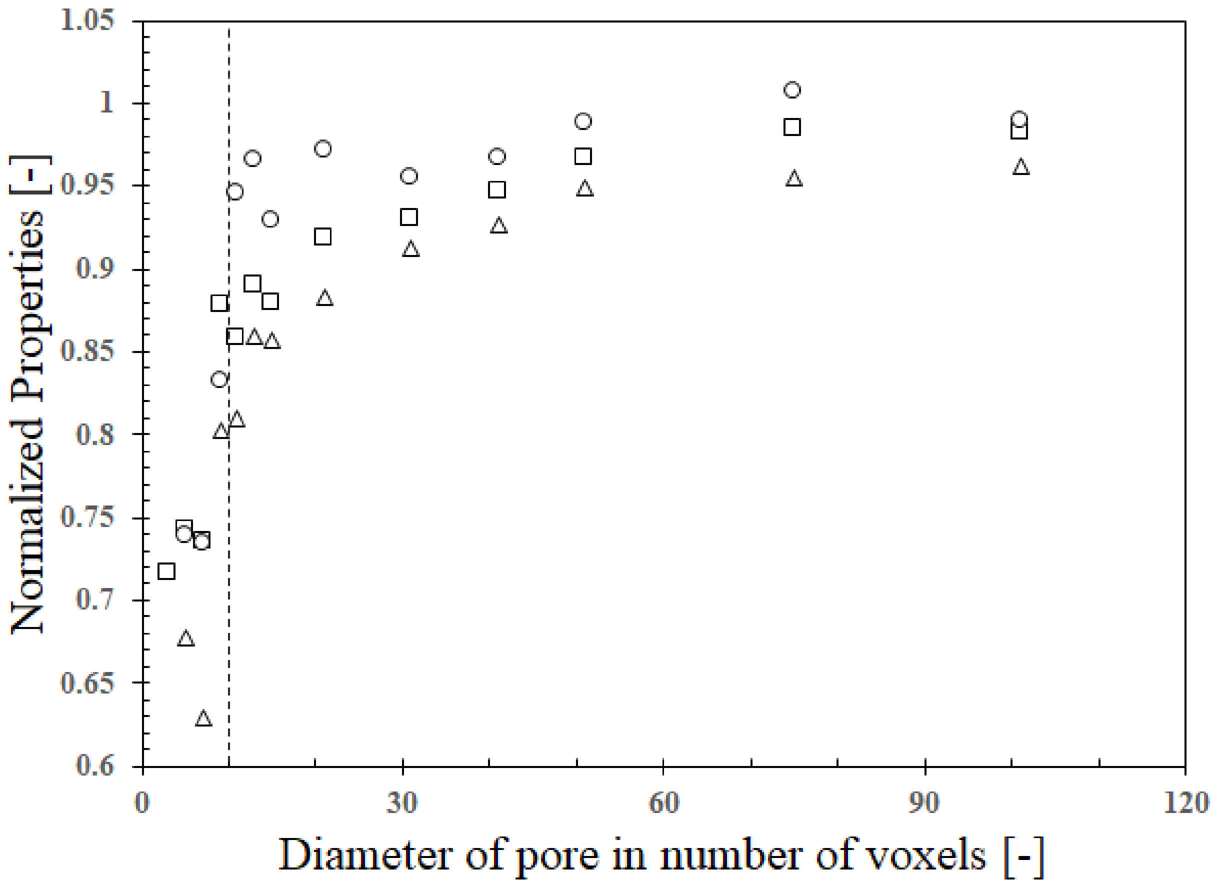

Figure 9. – Effect of image resolution (diameter of pore in number of voxel) on the evaluated pore properties: porosity (squares), specific surface area (triangles), and LBM permeability (circles). The properties are normalized by the corresponding analytical values. The vertical dotted line indicates a threshold value of the resolution below which the difference of the measured permeability with the analytical value is higher than 10%.

4. Discussion

4.1. Permeability variability

Within the studied DBs different processes could take places such as cementation, pressure solution, cataclasis, and shearing along sharp discontinuities. The DB hosted in SVG presents well-differentiated tabular zones where pore-network varies due to different processes. The cementation process generally occurs in the outer zone of the band, ZIII, characterized by the precipitation of cement and absence of pore-throat collapsing (Tondi, 2007). According to the observations, the permeability is negligible due to the isolation caused by the cementation. The only porosity in this zone reported by Zambrano *et al.* (2017) corresponds to isolated pores such as chambers within the bioclast, which do not contribute to the fluid flow. In the case of ZII, the compaction may cause the reduction of the primary pore-connectivity by collapsing the pore-throats. However, the same process also generates stylolites by pressure solution at the grain-to-grain contact (Tondi, 2007). It was observed that these stylolites, possible enlarged by dissolution, create thin pore conduits preferably connected to the DB. Due to the cataclastic nature of ZI, connected pores, if are present, may be below the resolution of the images and therefore not detected. However, if this is the case, the contribution to the permeability should of minor importance. Within the ZI, the fluid flow is possible through the space generated by the distribution of asperities within the slip surfaces. This pore network is characterized by wide and anastomose conduits that concentrate the fluid flow through the sharp discontinuity. The contribution to the permeability of the sharp discontinuity is very important in parallel direction of the DB. In fact, the total permeability of the FC reaches values just one order of magnitude less than the porous host rock in that direction. The permeability in an orthogonal direction to the DB is negligible due to the presence of ZI and ZII. Basically, the hydraulic behavior of the DB could be considered as a fracture surrounded by tight walls. This characteristic may have some implications to the modeling of those structures during the reservoir characterization.

In the case of the fault core sample of FIG (FIG-S3), there are not differentiated zones like in the DB form SVG. However, in this fault core there is an alternation of zones affected by cementation and dissolution, which are oriented subparallel to the main fault direction. The variability is well represented by great values of coefficient of variation especially in the z-direction (Cv=2.8), which indicates a high heterogeneity (Zhang *et al.*, 2000). This variability may be caused by localized cementation, compaction, dissolution and cataclasis. Moreover, the sample presents a high permeability anisotropy due to the fact that the fluid flow is only allowed subparallel to the fault and inhibited in the perpendicular direction. Comparing to the host rock (FIG-S2), the permeability values in the parallel direction are reduced by about two orders of magnitude.

In the samples from FIG, there is a slight variation of permeability in the deformed areas with respect to the pristine rock. There is neither an important anisotropy in the permeability. However, the values of the coefficient of variation are slightly higher in the FIG-S5 in comparison to FIG-S4 indicating a greater heterogeneity of the permeability. The interpretation of these results is that the deformation band is incipient with a minor effect on the permeability distribution.

In the host rocks the permeability is mostly isotropic. Some minor differences among permeability components related to changes in the texture of the pores and grain size composing the rocks. Considering the open discussion made by Tondi (2016), we may confirm that the permeability is controlled by the grains/pores size and the tortuosity of the

4.2. Dependency of permeability on connected pore-network properties

As it was expected, results indicated that the permeability seems proportional to the effective porosity and inversely proportional to both the specific surface area and the tortuosity (Fig.8a-c). The specific surface area has a very important effect on the permeability due to a greater surface in contact with the fluid that causes more friction to fluid motion. The dependency of permeability on the aforementioned pore-network properties has been previously stated by several authors (e.g. Kozeny, 1927; Carman, 1937; Archie, 1942; Wyllie and Rose, 1950; Swanson, 1981; and Katz and Thompson, 1986). In a closer case, the control exerted by these properties have been claimed by Tondi *et al.* (2016) to explain permeability differences in three orders of magnitude between porous carbonate grainstones pertaining to FIG and OFG.

Even though our intention was not to prove the validity of the Kozeny-Carman equation, the estimated permeability with this method was plotted against the LBM permeability (Fig. 8d). In general, the data shows an important scatter and seems not to fit properly to the equality line (k_{LBM}=k_{KC}). It was noticed that this scatter seems to be higher in the VOIs pertaining to deformed/diagenetized zones than in the host rocks VOIs and follow a different trend (Fig. 8d).

4.3. Validity and representativeness of results

The heterogeneity of the analyzed rocks has been described by the coefficient of variability (Cv). Zhang *et al.* (2000) indicated that a low Cv indicates that the results could be considered as representative statistically, which made it a good substitute of the well-known concept of REV. Considering the nature of the simulation experiments, the use of a statistical approach to find representative results is less straightforward and faster than to consider bigger volumes. The heterogeneity varies in function of the measured properties and the type of rock (i.e. HR and DB). In general, the permeability presents more variability with respect to the porosity, specific surface area and tortuosity. This stands to reason, because the permeability is depending of such properties (eq. 1). Mostaghimi *et al*. (2013) found comparable results, in which they concluded that the representativeness of a volume depends upon the evaluated property. As it was expected, the DB samples are more variable than the pristine rocks. This is related to the presence of bands or zones dominated by cementation, cataclasis or dissolution. The alternation of such bands may cause a high variability in all properties, especially in the permeability in the z-direction (perpendicular to the DB/fault plane). Considering these results, we consider that a larger number of samples are necessary to provide representative results for applications in reservoir simulation. However, for the scope of this work the variability was useful to characterize the heterogeneity and its implications at the pore scale.

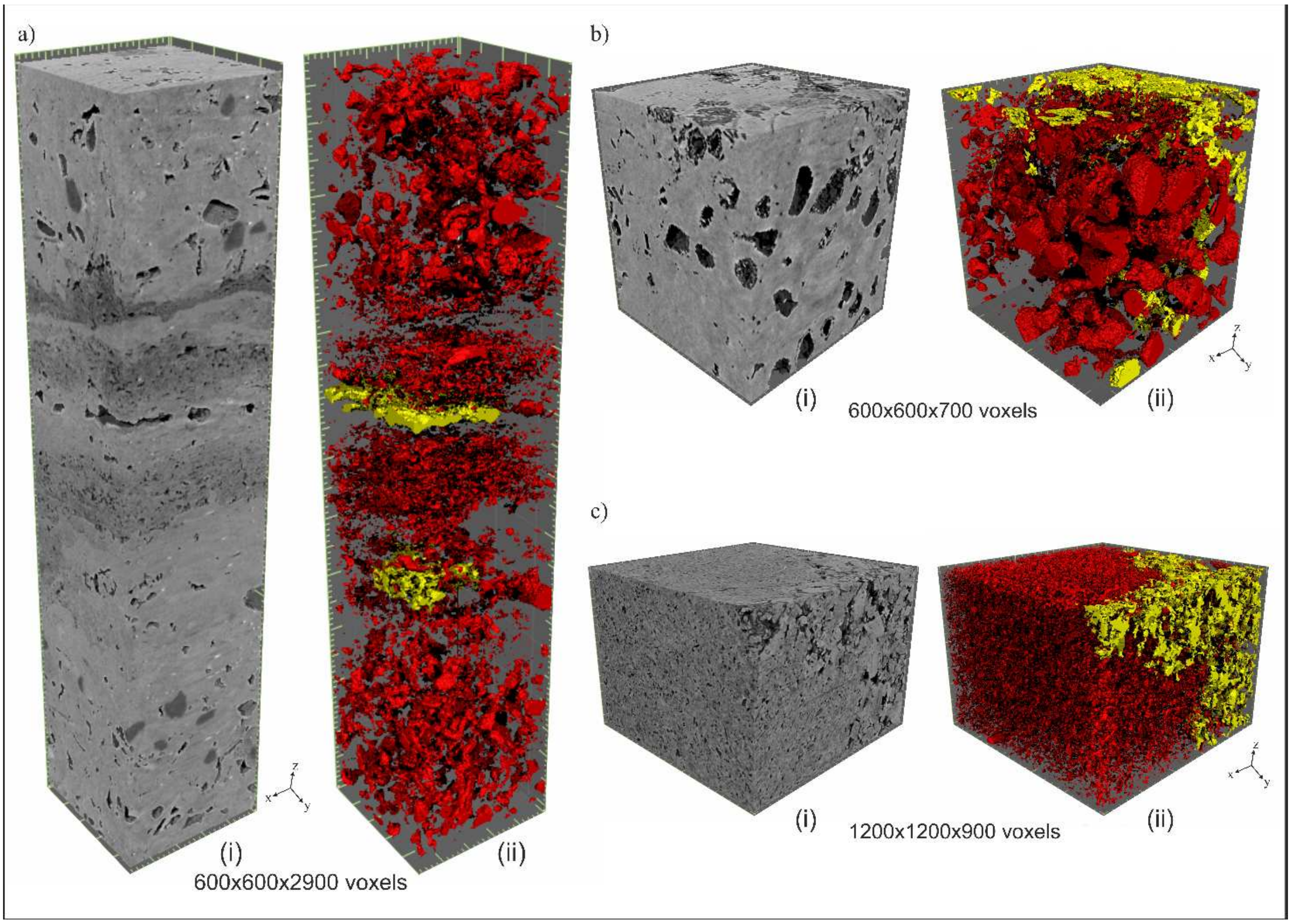

Figure 10.- DBs volumes at high resolution (voxel size = 2.4 µm) pertaining to a) Sample SVG-S1, b) Sample FIG-S3, and c) Sample OFG-S5. For each volume it is shown the (i) raw reconstructed SR micro-CT images and (ii) segmented pores space (connected pores in yellow and unconnected pores in red, after Zambrano et al. 2017). The z-axis of the volumes is perpendicular to the DB.

This study did not aim at providing exact values of permeability or to prove the accuracy of the LBM. However, permeability results are similar (one order of magnitude of difference) to the data obtained *in situ* by Antonellini *et al.* (2014) and Tondi *et al.* (2016) using an air permeameter. Nevertheless, it is necessary to take into consideration that these authors provided an important number of measurements and covered a total volume significantly greater than in the present work. On the other hand, the permeability obtained using an air permeameter may be also inaccurate. Filomena *et al.* (2014) reported that this technique applied to unconfined rock volumes (e.g. outcrop measurements) may be overestimated (about 37%) due to the shorter flow trajectories and a reduced rock volume in comparison with confined volume methods.

A key point for the validity of the results is the resolution of the images (voxel size = 9 μm) used for simulations. Even though higher resolution images (voxel size = 2.4 μm) were available, not connected pores were detected in the cemented zones within the DBs (Fig. 10). While, in both host rocks and zones affected by dissolution pores the pores are significantly wide (more than 100 μm). In agreement with Arzilli et al. (2015), studying similar grainstones of the Bolognano Fm., it is assumed that the contribution of the micropores to the permeability may be negligible if compared to the one of macropores. Nevertheless, the shape of imaged pores may be pixelated due to the resolution of the images affecting the measured properties (i.e. porosity, specific surface area, and permeability). In fact, these properties varied significantly in function of the resolution as it was found for a single pore evaluation (Fig. 9). The permeability seems to be constant and close to the theoretical value until certain threshold is reached (about 10 voxels of diameter). This result may be explained as a sort of compensation of the contrary effect on permeability exerted by the porosity and the specific surface area. Therefore, our results could infer that the presence of pores with a diameter lower than 100 μm may cause an underestimation of the permeability. Based on these evidence, the measured properties, including the permeability, may be slightly underestimated. However, the method used in this study and the results obtained allowed us to obtain textural and petrophysical properties of realistic rocks with a tensorial approach. In addition, it was put in evidence the control exerted by the textural properties on permeability within deformed rocks.

5. Conclusions

The presented study used the lattice-Boltzmann method (LBM) for obtaining permeability values of deformed carbonate grainstones using segmented 3D images obtained by synchrotron X-ray microtomography. The experiments consisted of inducing pressure-driven flow through the virtual rock samples and deriving the permeability by means of the Darcy's law.

The permeability and effective porosity decrease within deformation bands (DBs) due to the combination of grain translation, rotation, compaction, cataclasis, and cementation processes. Pore-throats are collapsed and occluded by processes mentioned above. The remaining porosity does not contribute to fluid flow as it is mostly isolated. In the zone III, the cement could fully occlude the pore network resulting in a local barrier for fluid flow in the direction perpendicular to the DB/fault. In the zone II, the compaction likely causes intergranular pore collapsing but when pressure dissolution takes places the resulting stylolites may contribute to the fluid flow, especially in the directions subparallel to the DB/fault. Concerning the zone I, the grain size reduction contributes to the occlusion of the intergranular pores. These processes could lead to negligible permeability values within the cataclastic zone. However, if sharp discontinuities are present, the distribution of asperities within the wall surfaces could cause a local enhancement of permeability parallel to the DB/fault and negligible to the orthogonal direction. In consequence, the permeability is highly anisotropic allowing the fluid flow only parallel to the DB similar to a fracture.

Our results indicate that permeability depends on the different evaluated properties (i.e. effective porosity, specific surface area and tortuosity). Permeability is directly related to the effective porosity, and inversely related to the specific surface area and the tortuosity. In the case of DBs, where rock volumes are affected by cementation and cataclasis, the permeability obtained by the LBM differs to the K-C.

Acknowledgements

This research was supported by the FAR Project 2014 “Characterization and modelling of natural reservoirs of geofluids in fractured carbonate rocks”, funded by the University of Camerino, Principal investigator E. Tondi and the Reservoir Characterization Project (www.rechproject.com). It is acknowledged the EXTREMA COST Action MP 1207 for networking support. Authors acknowledge the four anonymous reviewers for a very fair and critical revision of this manuscript. We also appreciate the patience showed by the editor and the reviewers during the revision taking into account the special circumstances. Finally, we thanks Alan Pitts and Hannah Riegel (University of Camerino) for the support during the revision of the manuscript.

References

Abrami, A.; Arfelli, F.; Barroso, R. C.; Bergamaschi, A.; Billè, F.; Bregant, P.; … Zanini, F., 2005. Medical applications of synchrotron radiation at the SYRMEP beamline of ELETTRA. Nucl. Instrum. Methods Phys. Res. 548, 221-227.

Adler P.M., Jacquin, C.G., and Quinlier, J.A., 1990. Flow in simulated porous media. Int. J. Multiphase Flow, 16, 691

Agosta, F., Prasad, M., Aydin, A., 2007. Physical properties of carbonate fault rocks, Fucino basin (Central Italy): implications for fault seal in platform carbonates. Geofluids 7, 19-32. http://dx.doi.org/10.1111/j.1468-8123.2006.00158.x.

Ahrenholz, B., Tölke, J., Lehmann, P., Peters, A., Kaestner, A., Krafczyk, M., and Durner, W., 2008. Prediction of capillary hysteresis in a porous material using lattice Boltzmann methods and comparison to experimental data and a morphological pore network model, Adv. Water Resour. 31, 1151-1173, doi:10.1016/j.advwatres.2008.03.009.

Ahrens, J., Geveci, B., Law, C., 2005. ParaView: An End-User Tool for Large Data Visualization, Visualization Handbook, Elsevier, ISBN-13: 978-0123875822

Al-Raoush, R., Papadopoulos, A., 2010., Representative elementary volume analysis of porous media using X-ray computed tomography. Powder Technol 200:69–77

American Petroleum Institute (API), 1998. Recommended Practices for Core Analysis, Recommended Practice 40, 2nd edn. API, Dallas, TX.

Andrä, H., Combaret, N., Dvorkin, J., Glatt, E., Han, J., Kabel, M., Keehm, Y., … Zhan, X., 2013. Digital rock physics benchmarks—part II: computing effective properties. Comput. Geosci. 50, 33–43. http://dx.doi.org/10.1016/j.cageo.2012.09.008.

Antonellini, M., Aydin, A., 1994. Effect of faulting on fluid flow in porous sandstones: petrophysical properties. AAPG Bulletin 78, 355-377. doi:10.1016/0148-9062(96)83981-7.

Antonellini, M., Cilona, A., Tondi, E., Zambrano, M., Agosta, F., 2014. Fluid flow numerical experiments of faulted porous carbonates, Northwest Sicily (Italy). Marine and Petroleum Geology, 55: 185-201, doi:10.1016/j.marpetgeo.2013.12.003.

Archie, G. E., 1942. The Electrical Resistivity Log as an Aid in Determining Some Reservoir Characteristics. Trans., AIME, 146, 54-62.

Arzilli, F., Cilona, A., Mancini, L., Tondi, E., 2015. Using synchrotron X-ray microtomography to characterize the pore network of reservoir rocks: a case study on carbonates. Advances in Water Resources. doi:10.1016/j.advwatres.2015.07.016.

Aydin, A., 1978. Small faults formed as deformation bands in sandstone. Pure and Applied Geophysics 116, 913-930. doi:10.1007/BF00876546.

Bear, J., 1972. Dynamics of fluids in porous media. Elsevier, New York.

Bhatnagar, P.L., Gross E.P., Krook M., 1954. A model for collision processes in gases. I: small amplitude processes in charged and neutral one-component system. Phys. Rev. 94, 511-525

Bijeljic B, Mostaghimi P, Blunt M.J., 2011. The signature of non-Fickian transport in highly heterogeneous media. Phys Rev Lett 107:204502

Bijeljic, B., Raeini, A., Mostaghimi, P., Blunt, M.J., 2013. Predictions of non-Fickian solute transport in different classes of porous media using direct simulation on pore-scale images. Phys. Rev.E 87(1), 013011. doi:10.1103/PhysRevE.87.013011

Blunt, M. J., Bijeljic, B., Dong, H., Gharbi, O., Iglauer, S., Mostaghimi, P., Paluszny, A., and Pentland, C. H., 2013. Pore-scale imaging and modeling. Adv. Water Resour., 51, 197–216.

Boek E.S., Venturoli M., 2010. Lattice-Boltzmann studies of fluid flow in porous media with realistic rock geometries. Comput. Math. Appl.; 59 (7): 2305-2314.

Brun, F., Mancini, L., Kasae, P., Favretto, S., Dreossi, D., Tromba, G., 2010. Pore3D: a software library for quantitative analysis of porous media. Nucl. Instrum. Meth A 615, 326-332. http://dx.doi.org/10.1016/j.nima.2010.02.063.

Brun, F., Pacilè, S., Accardo, A., Kourousias, G., Dreossi, D., Mancini, L., Tromba, G., Pugliese, R., 2015. Enhanced and Flexible Software Tools for X-ray Computed Tomography at the Italian Synchrotron RadiationFacility Elettra. Fundamenta Informaticae 141(2015) 233–243.

Bultreys, T., de Boever, W., and Cnudde, V. 2016. Imaging and image-based fluid transport modeling at the pore scale in geological materials: A practical introduction to the current state-of-the-art. Earth Sci. Rev. 155:93–128. doi:10.1016/j.earscirev.2016.02.00

Cardenas, M. B., 2008. Three-dimensional vortices in single pores and their effects on transport. Geophys. Res. Lett., 35, L18402, doi:10.1029/ 2008GL035343.

Cardenas, M. B., 2009. Direct simulation of pore level Fickian dispersion scale for transport through dense cubic packed spheres with vortices. Geochem. Geophys. Geosyst., 10, Q12014, doi:10.1029/2009GC002593.

Carman, P.C., 1937. Fluid flow through granular beds. Trans. Inst. Chem. Eng. 15, 150.

Cerepi, A., Humbert, L., Burlot, R., 2001. Petrophysical properties of porous medium from Petrographic Image Analysis data. Colloids and Surfaces. A: Physicochemical and Engineering Aspect, 187-188, 233-256.

Chen, S., and Doolen, G. D.,1998. Lattice Boltzmann method for fluid flows. Annu. Rev. Fluid Mech.; 30:329-364.

Cilona, A., Baud, P., Tondi, E., Agosta, F., Vinciguerra, S., Rustichelli, A., Spiers, C.J., 2012. Deformation bands in porous carbonate grainstones: field and laboratory observations. Journal of Structural Geology, 45, 137-157.

Cilona, A., Faulkner, DR., Tondi, E., Agosta, F., Mancini, L., Rustichelli, A., Baud, P., Vinciguerra, S., 2014. The effects of rock heterogeneity on compaction localization in porous carbonates. J Struct Geol, 67: 75-93, doi:10.1016/j.jsg.2014.07.008.

Cloetens, P., Barrett, R., Baruchel, J., Guigay, J.P., Schlenker, M., 1996. Phase objects in synchrotron radiation hard X-ray imaging. J Phys D Appl Phys, 29: 133-146, doi:10.1088/0022-3727/29/1/023

Coelho, D., Thovert, J.-F., and Adler P. M., 1997. Geometrical and transport properties of random packings of spheres and aspherical particles. Phys. Rev. E, 55, 1959–1978.

Degruyter, W., Burgisser, A., Bachmann, O., Malaspinas, O., 2010. Synchrotron X-ray microtomography and lattice Boltzmann simulations of gas flow through volcanic pumices. Geosphere, v. 6, no. 5, p. 470-481, doi: 10.1130/GES00555.1.

d'Humières, D., 1992. Generalized Lattice-Boltzmann equations, in: Rarefied Gas Dynamics: Theory and Simulations, Prog. Astronaut. Aeronaut., vol. 159, edited by B. D. Shizgal and D. P. Weave, pp. 450-458, AIAA, Washington, D. C.

d'Humières, D., Ginzburg, I., Krafczyk, M., Lallemand P., and Luo., L-S., 2002. Multiple-Relaxation-Time Lattice Boltzmann Models in Three Dimensions, Phil. Trans. R. Soc. A, 360, 437-451.

Dullien, F. A. L., 1992. Porous Media: Fluid Transport and Pore Structure, 574 pp., Academic, San Diego, Calif.

Dunsmuir, J.H., Ferguson, S.R., D'Amico, K.L., Stokes, J.P., 1991. X-ray microtomography: a new tool for the characterization of porous media, paper SPE 22860. Proceedings of the 1991 SPE Annual Technical Conference and Exhibition, Dallas, October 6-9.

Filomena, C., Hornung, J., and Stollhofen, H., 2014. Assessing accuracy of gas-driven permeability measurements: a comparative study of diverse Hassler-cell and probe permeameter devices. Solid Earth 5, 1–11. doi: 10.5194/se-5-1-2014

Fossen, H., & Bale, A., 2007. Deformation bands and their influence on fluid flow. AAPG Bulletin 91, 1685-1700.

Fossen, H., Schultz, R.A., Shipton, Z.K., Mair, K., 2007. Deformation bands in sandstone: a review. J. Geol. Soc. 164, 755e769. http://dx.doi.org/10.1144/0016-76492006-036.

Fredrich, J.T., DiGiovanni, A.A., Noble, D.R., 2006. Predicting macroscopic transport properties using microscopic image data. J. Geophys. Res. 111, B03201. http://dx.doi.org/10.1029/2005JB003774

Gaviglio, P., Bekri, S., Vandycke, S., Adler, P.M., Schroeder, C., Bergerat, F., Darquennes, A., & Coulon, M. 2009. Faulting and deformation in chalk. Journal of structural geology, 31, 194-207.

Ghanbarian, B., Hunt, A.G., Ewing, R.P., and Sahimi. M., 2013. Tortuosity in porous media: A critical review. Soil Sci. Soc. Am. J. 77:1461-1477, doi:10.2136/sssaj2012.0435

Gharbi, O., and Blunt, M.J., 2012, The impact of wettability and connectivity on relative permeability in carbonates: A pore network modelling analysis, Water Resour. Res., 48, W12513, doi:10.1029/2012WR011877.

Gommes, C. J., Bons, A.J., Blacher, S., Dunsmuir, J.H. and Tsou, A.H., 2009. Practical methods for measuring the tortuosity of porous materials from binary or gray-tone tomographic reconstructions. AIChE J., 55: 2000-2012. doi:10.1002/aic.11812.

Graham, B., Antonellini, M., Aydin, A., 2003. Formation and growth of normal faults in carbonates within a compressive environment, Geology, 31, 11-14.

Gürsoy, D., De Carlo, F., Xiao, X., Jacobsen, C., 2014. TomoPy: a framework for the analysis of synchrotron tomographic data, Journal of Synchrotron Radiation, 21(5), 1188-1193.

Hao, L., Cheng, P., 2010. Pore-scale simulations on relative permeabilities of porous media by lattice Boltzmann method. Int. J. Heat Mass Transfer;53(9– 10):1908–1913.

Hartigan, J.A., 1975. Clustering Algorithms. Wiley, New York.

Hartigan, J.A., Wong, M.A., 1979. A K-means clustering algorithm. Appl. Stat. 28, 100-108.

Hellmann, R., Renders, P. J. N., Gratier J. P. , and Guiguet, R., 2002. Experimental pressure solution compaction of chalk in aqueous solutions Part 1, Deformation behavior and chemistry, in: R. Hellmann, S. A. Wood, Water-Rock Interaction, Ore Deposits, and Environmental Geochemistry: A Tribute to David A. Crerar, The Geochemical Society, Special Publication 7, 129-152.

Jin, G., Patzek, T.W., Silin, D.B., 2004. Direct prediction of the absolute permeability of unconsolidated consolidated reservoir rock. In: Proceedings of the SPE annual technical conference exhibition, Houston, TX. (SPE 90084)

Kang, Q., Lichtner, P.C., Zhang, D., 2006. Lattice Boltzmann pore-scale model for multicomponent reactive transport in porous media. J Geophys Res;111:B05203.

Katz, A. J., and Thompson, A. H., 1986. Quantitative Prediction of Permeability in Porous Rock. Phys. Rev. B, 34, 8179-81.

Keehm, Y., 2003. Computational rock physics: Transport properties in porous media and applications, Ph.D. Dissertation, 135 pp., Stanford Univ., Stanford, Calif.

Keehm, Y., Mukerji, T., Nur A., 2001. Computational rock physics at the pore scale: Transport properties and diagenesis in realistic pore geometries, The Leading Edge, 20, 180-183.

Keehm, Y., Mukerji, T., Nur, A., 2004. Permeability prediction from thin sections: 3D reconstruction and Lattice-Boltzmann flow simulation. Geophys. Res. Lett., 31, L04606, doi:10.1029/2003GL018761.

Khan, F., Enzmann, F., Kersten, M., Wiegmann, A., Steiner, K., 2012. 3D simulation of the permeability tensor in a soil aggregate on basis of nanotomographic imaging and LBE solver. J. Soils Sediments 12, 86–96. http://dx.doi.org/10.1007/s11368-011-0435-3.

Kozeny J., “Uber Kapillare Leitung des Wassers im Boden, Sitzungsber,” Akad. Wiss. Wien, Math. Naturw Klasse, Abt.II A, 1927, 136, 271-306.

Ladd, A. J. C., 1994. Numerical simulations of particulate suspensions via a discretized Boltzmann equation: Part 2. Numerical results, J. Fluid Mech., 271, 311-339.

Landry, C.J., Karpyn, Z.T., Ayala, O., 2014. Relative permeability of homogenous-wet and mixed-wet porous media as determined by pore-scale lattice Boltzmann modeling. Water Resour. Res. 50, 3672–3689. http://dx.doi.org/10.1002/2013WR015148.

Latt, J., 2009, Palabos, Parallel Lattice Boltzmann Solver: http://www.lbmethod.org/palabos/

Li, Y., LeBoeuf, E. J., Basu, P. K., & Mahadevan, S., 2005. Stochastic modeling of the permeability of randomly generated porous media. Advances in Water Resources, 28(8), 835-844.

Lucia, F.J., 2007. Carbonate Reservoir Characterization: an Integrated Approach. Springer Science & Business Media.

Manwart, C., Aaltosalmi, U., Koponen, A., Hilfer, R., and Timonen J., 2002. Lattice-Boltzmann and finite-difference simulations for the permeability for three-dimensional porous media, Phys. Rev. E, 66, 016702, doi:10.1103/ PhysRevE.66.016702.

Manz, B., Gladden, L. F., and Warren, P. B., 1999. Flow and dispersion in porous media: Lattice Boltzmann and NMR studies, AIChE J., 45, 1845-1854.

Mostaghimi, P., Bijeljic, B., and Blunt, M. J., 2012. Simulation of flow and dispersion on pore-space images, SPE J., 17(4), 1131–1141.

Mostaghimi, P., Blunt, M.J., Bijeljic, B., 2013. Computations of absolute permeability on micro-CT images. Math. Geosci., 45, pp. 103-125

Mutti, M., 1995. Porosity development and diagenesis in the Orfento supersequence and its bounding unconformities (Upper Cretaceous, Montagna Della Majella, Italy). American Association of Petroleum Geologists Special Publications, 141-158.

Narvaez, A., Zauner, T., Raischel, F., Hilfer, R., and Harting, J., 2010. Quantitative analysis of numerical estimates for the permeability of porous media from lattice-Boltzmann simulations, J. Stat. Mech., 11, P11026.

Øren, P.E., and Bakke, S., 2002. Process based reconstruction of sandstones prediction of transport properties. Transp Porous Media 46:311–343

Ori, G.G., Roveri, M., Vannoni, F., 1986. Plio-Pleistocene sedimentation in the Apennine–Adriatic foredeep (central Adriatic Sea, Italy). In: Allen, P.A., Homewood, P. (Eds.), Foreland Basins. Blackwell, Oxford, pp. 183–198.

Palenstijn, W., Batenburg, K., Sijbers, J., 2011. Performance improvements for iterative electron tomography reconstruction using graphics processing units (GPUs), Journal of Structural Biology, 176(2), 2011, 250-253.

Pan, C., Hilpert, M., Miller, C.T., 2004. Lattice-Boltzmann simulation of two-phase flow in porous media. Water Resour Res; 40:W01501.

Pan, C., Luo, L.S., & Miller, C.T., 2006. An evaluation of lattice Boltzmann schemes for porous medium flow simulation. Computers & fluids, 35(8), 898-909.

Peng, S., Marone, F., Dultz, S., 2014. Resolution effect in X-ray microcomputed tomography imaging and small pore's contribution to permeability for a Berea sandstone. J. Hydrol. 510, 403–411. http://dx.doi.org/10.1016/j.jhydrol.2013.12.028.

Porter, M.L., Schaap, M.G., Wildenschild, D., 2009. Lattice-Boltzmann simulations of the capillary pressure–saturation–interfacial area relationship for porous media. Adv Water Resour; 32(11):1632–40.

Rustichelli, A., Torrieri, S., Tondi, E., Laurita, S., Strauss, C., Agosta, F., Balsamo, F., 2016. Fracture characteristics in cretaceous platform and overlaying ramp carbonates: an outcrop study from Maiella mountain (central Italy). Mar. Petroleum Geol. 76, 68-87.

Schaap, M.G., Porter, M.L., Christensen, B.S.B., Wildenshild, D., 2007. Comparison of pressure-saturation characteristics derived from computed tomography and lattice Boltzmann simulations. Water Resour Res ; 43:W12S06.

Schindelin, J., Arganda-Carreras, I., Frise, E., *et al.*, 2012. Fiji: an open-source platform for biological-image analysis. Nat. methods 9 (7), 676-682.

Shah, S.M., Gray, F., Crawshaw, J.P., Boek, E.S., 2015. Micro-computed tomography porescale study of flow in porous media: effect of voxel resolution. Adv. Water Resour. 000, 1–12. http://dx.doi.org/10.1016/j.advwatres.2015.07.012.

Soille, P., 1999. Morphological Image Analysis, Principles and Application. Berlin: Springer.

Spanne, P., Thovert, J. F., Jacquin, C. J., Lindquist, W. B., Jones, K. W., & Adler, P. M., 1994. Synchrotron computed microtomography of porous media: topology and transports. Physical Review Letters, 73(14), 2001.

Stapf, S., Packer, K. J., Bèkri, S., and Adler, P. M., 2000. Two-dimensional nuclear magnetic resonance measurements and numerical simulations of fluid transport in porous rocks. Phys. Fluids, 12(3), 566–580, doi:10.1063/1.870262.

Sukop, M.C., Huang, H., Lin, C.L., Deo, M.D., Oh, K., & Miller, J.D., 2008. Distribution of multiphase fluids in porous media: Comparison between lattice Boltzmann modeling and micro-x-ray tomography. Physical Review E, 77(2), 026710.

Swanson, B.F., 1981. A Simple Correlation Between Permeabilities and Mercury Capillary Pressures. J. Pet. Tech., 1, 33, 2498-2504.

Tessier, J. J., Packer, K. J., Thovert, J.-F., and Adler, P. M., 1997. NMR measurements and numerical simulation of fluid transport in porous solids, AIChE J., 43, 1653–1661.

Tomasi, C., Manduchi, R., 1998. Bilateral filtering for gray and color images. Sixth International Conference on Computer Vision, New Delhi, India, 839-846.

Tondi, E., 2007. Nucleation, development and petrophysical properties of faults in carbonate grainstones: evidence from the San Vito Lo Capo peninsula (Sicily, Italy). Journal of Structural Geology, 29, 614-628, doi:10.1016/j.jsg.2006.11.006.

Tondi, E., Antonellini, M., Aydin, A., Marchegiani, L., Cello, G., 2006. The role of deformation bands, stylolites and sheared stylolites in fault development in carbonate grainstones of Majella Mountain, Italy. J Struct Geol, 28: 376-391, doi:10.1016/j.jsg.2005.12.001.

Tondi, E., Rustichelli, A., Cilona, A., Balsamo, F., Storti, F., Napoli, G., Agosta, F., Renda, P., Giorgioni, M., 2016. Hydraulic properties of fault zones in porous carbonates, examples from central and southern Italy. Italian Journal of Geosciences, Volume 135, f.1. 68-79. doi: 10.3301/IJG.2015.08

Tondi, E., Cilona, A., Agosta, F., Aydin, A., Rustichelli, A., Renda, P., Giunta, G., 2012. Growth processes, dimensional parameters and scaling relationships of two conjugate sets of compactive shear bands in porous carbonate grainstones, Favignana Island, Italy. J Struct Geol, 37: 53-64, doi: http://dx.doi.org/10.1016/ j.jsg.2012.02.003.

Tromba, G., Longo, R., Abrami, A., Arfelli, F., Astolfo, A., Bregant, P., …, Castelli E., 2010. The SYRMEP Beamline of Elettra: Clinical Mammography and Bio-medical Applications. AIP Conference Proceedings, 1266: 18-23.

Voltolini, M., Zandomeneghi, D., Mancini, L., Polacci, M., 2011. Texture analysis of volcanic rock samples: quantitative study of crystals and vesicles shape preferred orien- tation from X-ray microtomography data. J Volcanol Geoth Res; 202:83–95 http://dx.doi.org/10.1016/j.jvolgeores.2011.02.003.

Wildenschild, D., & Sheppard, A.P., 2013. X-ray imaging and analysis techniques for quantifying pore-scale structure and processes in subsurface porous medium systems. Advances in Water Resources, 51, 217-246. doi: 10.1016/j.advwatres.2012.07.018.

Wu, K., Dijke, M.I.J., Couples, G.D., Jiang, Z., Ma, J., Sorbie, K.S., Crawford, J., Young, I., Zhang, X., 2006. 3D stochastic modelling of heterogeneous porous media - applications to reservoir rocks. Transp. Porous Media 65, 443–467. http://dx.doi.org/10.1007/ s11242-006-0006-z.

Wyllie, M. R. J., and Rose, W., 1950. Some Theoretical Considerations Related to the Quantitative Evaluation of the Physical Characteristics of Reservoir Rock for Electrical Log Data. Trans., AIME, 189, 105-118.

Yang, X., Mehmani, Y., Perkins, W. A., Pasquali, A., Schönherr, M., Kim, K., ... & Richmond, M. C., 2016. Intercomparison of 3D pore-scale flow and solute transport simulation methods. Advances in Water Resources, 95, 176-189.

Yao, J., Thovert, J.-F., Adler, P. M., Tsakiroglou, C. D., Burganos, V. N., Payatakes, A. C., Moulu, J. C., and Kalaydjian, F., 1997. Characterization, reconstruction and transport properties of Vosges sandstones. Rev. Inst. Fr. Pet., 52(1), 3–21.

Zambrano, M., Tondi, E., Mancini, L., Arzilli, F., Lanzafame, G., Materazzi, M., & Torrieri, S., 2017. 3D Pore-network quantitative analysis in deformed carbonate grainstones. Marine and Petroleum Geology, 82, 251-264.

Zandomeneghi, D., Voltolini, M., Mancini, L., Brun, F., Dreossi, D., Polacci, M., 2010. Quantitative analysis of X-ray microtomography images of geomaterials: Application to volcanic rocks. Geosphere, 6: 793-804, doi: 10.1130/GES00561.1.

Zaretskiy, Y., Geiger, S., Sorbie, K., and Förster, M., 2010. Efficient flow and transport simulations in reconstructed 3D pore geometries. Adv. Water Resour., 33(12), 1508–1516.

Zhang, D., Papadikis, K., & Gu, S., 2016. A lattice Boltzmann study on the impact of the geometrical properties of porous media on the steady state relative permeabilities on two-phase immiscible flows. Advances in Water Resources, 95, 61-79.

Zhang, D., Zhang, R., Chen, S., and Soll, W.E., 2000. Pore scale study of flow in porous media: Scale dependency, REV, and statistical REV, Geophys. Res. Lett., 27, 1195-1198, doi:10.1029/1999GL011101.

Zhang, S., Klimentidis, R.E., Barthelemy, P., 2012. Micron to millimeter upscaling of shale rock properties based on 3D imaging and modeling. Int. Symp. Soc. Core Analysts. Society of Core Analysts.